



THE OXYGEN FEATURES IN TYPE Ia SUPERNOVAE AND IMPLICATIONS FOR THE NATURE OF THERMONUCLEAR EXPLOSIONS

XULIN ZHAO^{1,2,3}, KEIICHI MAEDA^{2,4}, XIAOFENG WANG¹, LIFAN WANG⁵, HANNA SAI¹, JUJIA ZHANG^{6,7}, TIANMENG ZHANG⁸,
FANG HUANG¹, AND LIMING RUI¹

¹ Physics Department and Tsinghua Center for Astrophysics, Tsinghua University, Beijing, 100084, China;
wang_xf@mail.tsinghua.edu.cn, zhaoxl11@mails.tsinghua.edu.cn

² Department of Astronomy, Kyoto University, Kitashirakawa-Oiwake-cho, Sakyo-ku, Kyoto 606-8502, Japan; keiichi.maeda@kustastro.kyoto-u.ac.jp

³ School of Science, Tianjin University of Technology, Tianjin, 300384, China

⁴ Kavli Institute for the Physics and Mathematics of the Universe (WPI), University of Tokyo, 5-1-5 Kashiwanoha, Kashiwa, Chiba 277-8583, Japan

⁵ Mitchell Institute for Fundamental Physics and Astronomy, Texas A&M University, College Station, TX 77843, USA

⁶ Yunnan Observatories, Chinese Academy of Sciences, Kunming, 650216, China

⁷ Key Laboratory for the Structure and Evolution of Celestial Objects, Chinese Academy of Sciences, Kunming 650216, China

⁸ National Astronomical Observatory of China, Chinese Academy of Sciences, Beijing, 100012, China

Received 2016 January 27; revised 2016 May 11; accepted 2016 May 23; published 2016 August 1

ABSTRACT

The absorption feature $O\ I\ \lambda 7773$ is an important spectral indicator for type Ia supernovae (SNe Ia) that can be used to trace the unburned material in outer layers of the exploding white dwarf (WD). In this work, we use a large sample of SNe Ia to examine this absorption at early phases (i.e., $-13\ \text{day} \lesssim t \lesssim -7\ \text{day}$) and make comparisons with the absorption features of $Si\ II\ \lambda 6355$ and the $Ca\ II$ near-infrared triplet. We show that for a subgroup of spectroscopically normal SNe with normal photospheric velocities (i.e., $v_{si} \lesssim 12,500\ \text{km s}^{-1}$ at optical maximum), the line strength of the high velocity feature (HVF) of $O\ I$ is inversely correlated with that of $Si\ II$ (or $Ca\ II$), and this feature also shows a negative correlation with the luminosity of SNe Ia. This finding, together with other features we find for the $O\ I$ HVF, reveal that for this subgroup of SNe Ia, explosive oxygen burning occurs in the outermost layer of the SN. Differences in the oxygen burning could lead to the observed diversity, which is in remarkable agreement with the popular delayed-detonation model of Chandrasekhar mass WDs.

Key words: methods: data analysis – supernovae: general – techniques: spectroscopic

1. INTRODUCTION

Type Ia supernovae (SNe Ia) are important in cosmology and astrophysics, not only for the key role they played in the discovery of the accelerating universe (Riess et al. 1998; Perlmutter et al. 1999), but also for their contribution to the production of heavy elements in the universe. However, the nature of their progenitor systems is still controversial (e.g., Maoz et al. 2014, and references therein). It is widely accepted that SNe Ia are the result of a thermonuclear explosion of carbon/oxygen (C/O) white dwarfs (WDs), but there are two major channels proposed so far that could lead to such an explosion. One is the explosion of a WD which accretes hydrogen or helium from its non-degenerate companion (the single degenerate scenario; Whelan & Iben 1973; Nomoto 1982; Nomoto et al. 1997), which is supported by the detection of circumstellar material (CSM) around some SNe Ia (Hamuy et al. 2003; Aldering et al. 2006; Patat et al. 2007; Sternberg et al. 2011; Dilday et al. 2012; Maguire et al. 2013; Silverman et al. 2013). The other is the merger of two WDs (the double degenerate scenario; Iben & Tutukov 1984; Webbink 1984), which has recently received more attention due to the observational findings that no companion signature is found for some SNe Ia, e.g., the nearby object SN 2011fe and some SN remnants such as SN 1006 and SNR 0509-67.5 in the LMC, down to luminosities much fainter than the Sun (Li et al. 2011; Bloom et al. 2012; Brown et al. 2012; Hernández et al. 2012; Schaefer & Pagnotta 2012).

There are also differences in the spectroscopic and photometric properties of SNe Ia, and researchers have considered whether all (or spectroscopically normal) SNe Ia originate in a single evolutionary path or whether there are

multiple populations. For example, there is the so-called high velocity (HV) subclass of SNe Ia (Wang et al. 2008; Wang et al. 2009a), with redder peak $B-V$ colors and slower late-time decline rates in bluer bands relative to the normal-velocity (Normal) subclass⁹, and it is interesting to explore whether these represent different populations. The observed differences between the HV and Normal SNe Ia could at least partly be attributed to the geometric effect of an asymmetric explosion (Maeda et al. 2010; Maund et al. 2010). However, the observed differences have also been found to be linked to birthplace environments, to some extent (Wang et al. 2013), suggesting that SNe Ia may arise from multiple classes of binary evolution. Taken together, this could mean that there are two populations in the HV subclass, one of which is related to Normal SNe Ia while the other is not.

The other long-standing problem is the physical process of SN Ia explosions (Hillebrandt & Niemeyer 2000). Theoretically, the thermonuclear reaction disrupting the star may propagate at a range of speeds from subsonic deflagration to supersonic detonation (Nomoto et al. 1984; Khokhlov 1991; Fink et al. 2010; Pakmor et al. 2012). The most popular scenario is the delayed-detonation model (Khokhlov 1991), which assumes that a strong detonation unbinds the whole progenitor WD, after a deflagration which produces stable Fe-peak elements near the center of the WD. Another popular model involves the double-detonation mechanism (Livne & Glasner 1990; Fink et al. 2007; Sim et al. 2012; Shen & Bildsten 2014). In this model, explosive He burning is induced

⁹ This spectroscopic classification is based on the photospheric velocity measured from $Si\ II\ \lambda 6355$ lines in the near-maximum-light spectra (Wang et al. 2009a).

on the WD surface by compressional heating if the accreted He amount is sufficiently large, and this creates a shock wave penetrating into the WD core. Once the shock wave converges near the center, a powerful detonation can be triggered and will lead to an explosion unbinding the whole WD. Existing observational diagnostics offer some clues for the explosion models, but this topic is still controversial.

The high-velocity absorption features (HVF) can provide evidence of the burning processes in the outer layers of the exploding WD, although their origins are still debated. The HVFs are absorption components that are likely formed in regions lying above the photosphere (Hatano et al. 1999; Mazzali et al. 2005b), with velocities $>16,000 \text{ km s}^{-1}$. The HVFs of the Ca II near-infrared (NIR) triplet and Si II 6355 Å in SNe Ia have been systematically examined using both early-phase and near-maximum-light spectra (Maguire et al. 2012; Childress et al. 2014; Silverman et al. 2015; Zhao et al. 2015). These studies indicate that the abundance distributions of Si and Ca are strongly related, likely as a result of the same burning process being responsible for creating Si and Ca. Since Si and Ca are basically produced in the same burning layer, their relative strengths are not expected to be sensitive to the typical burning process they experienced. It is thus interesting to make comparisons with absorption features created by elements whose abundance patterns are different from Si and Ca in different burning layers. C II 6580 could be an important indicator of unburned fuel in the progenitor and observations of this feature have been discussed in many studies (Parrent et al. 2011; Thomas et al. 2011; Blondin et al. 2012; Folatelli et al. 2012; Silverman & Filippenko 2012; Maguire et al. 2014; Hsiao et al. 2015). However, C II 6580 absorption is usually very weak and difficult to be quantified in terms of line strength and velocity distribution. The O I 7773 line, in contrast, is relatively strong but has not been explored so far. Thus, in this paper, we propose using this feature as a tracer of unburned material, although some oxygen is also produced via carbon burning.

The presence of HVFs in O I 7773 absorption has only been reported in the earliest spectra of SN 2011fe in M101, where it was observed to disappear rapidly (Nugent et al. 2011). Detection of such an O-HVF is critically important, since Si and Ca are produced from O via oxygen burning, and the comparison of the HVFs of O and those of Si and Ca can potentially be used to confirm their associations. In the Si burning layer oxygen is fully consumed; in the O burning layer O, Si, and Ca can have large abundances; in the C burning layer oxygen is abundant, but Si and Ca are under-abundant; and finally, in the unburned layer the ratio of O to Si or Ca is large. Thus, we may obtain information about the typical burning process encountered by the layer producing the HVFs, and hence the still-unclarified origin of the outermost materials in SN Ia.

This paper is organized as follows. In Section 2, our data samples and methods for measuring the spectral parameters are introduced. In Section 3, correlations between the spectroscopic parameters of oxygen (O I 7773) and those of other elements (Si II 6355, Ca II NIR triplet, and C II 6580) are investigated. Correlations between the spectroscopic features of O I 7773, Si II 6355, the Ca II NIR triplet, and luminosity indicator $\Delta m_{15}(B)$ are also examined and analyzed in this section. The origins of HVFs and the constraints on explosion models are discussed in Section 4. A conclusion is given in Section 5.

2. DATA SET AND METHODS OF MEASUREMENT

2.1. Sample

Since the HVFs of SNe Ia are only prominent in their early spectra, we choose a sample with spectroscopic observations at $t \lesssim -7$ day from the B-band maximum light. Our sample is taken from the published spectral data bases of the CfA Supernova Program (Matheson et al. 2008; Blondin et al. 2012), the Berkeley Supernova Program (Silverman et al. 2012a), and the Carnegie Supernova Project (CSP: Folatelli et al. 2013), and the unpublished data set from the Tsinghua Supernova Program.¹⁰ The telluric absorption features were removed from almost all of the spectral samples above using the standard-star spectra obtained with the same slit used for the SN observations. However, this procedure often leaves residuals from the strongest telluric bands near 7620 Å. With the multi-Gaussian fit addressed in the next subsection, we examine the blending of the residual telluric absorption with the O I 7773 absorption in the spectra of our SN Ia sample. The spectra showing larger degrees of blending between these two absorptions (see Section 2.2) are excluded from our analysis. Moreover, the near-maximum-light Si II 6355 velocity is also required for further classification of our sample. This leads to a total of 143 early-time spectra (with $t \lesssim -7$ day from the B-band maximum light) that cover the wavelength region of O I 7773 absorption. These spectra belong to 62 SNe Ia, including 55 spectroscopically normal SNe Ia, two 1991T-like SNe (Filippenko et al. 1992; Phillips et al. 1992), and five 1999aa-like SNe Ia (Li et al. 2001) (hereafter these two subclasses are abbreviated to 91T/99aa-like SNe Ia). The spectroscopically normal objects can be further divided into 42 Normal SNe Ia and 13 HV ones.

The above sample of SNe Ia were largely included in our previous study (Zhao et al. 2015), where their photometric and host-galaxy parameters (i.e., $\Delta m_{15}(B)$, $B_{\text{max}} - V_{\text{max}}$, spectroscopic subclassification, host-galaxy type, K-band magnitude of the host galaxy, etc.) can be found. The sources of the light curves are from the Harvard CfA Supernova Group (Hicken et al. 2009, 2012), the CSP (Contreras et al. 2010; Stritzinger et al. 2011), the Lick Observatory Supernova Search (Ganeshalingam et al. 2010), and our own database.

2.2. Measurement Procedure

The measurement procedure of O I absorption is similar to that applied to measuring the Si II 6355/5972 and Ca II NIR triplet absorptions (Zhao et al. 2015), but with more Gaussian components being used to fit more absorptions. The absorptions identified around O I 7773 include three O I components (two HVFs and one photospheric component), three residual telluric components (i.e., at λ_s 7186, 7606, 7630 Å), and a possible Mg II 7890 component (with a velocity at $10,000 \text{ km s}^{-1} \sim 14,000 \text{ km s}^{-1}$). These absorption components can be represented using the following multi-component Gaussian function:

$$f(\lambda) = \sum_{i=1}^6 A_i \exp\left(-\frac{(\lambda_i - \lambda_i^0)^2}{2\sigma_i^2}\right) \quad (1)$$

¹⁰ This data set contains nearly 1000 spectra for over 200 SNe (L. Rui et al. 2016, in preparation), obtained with the Lijiang 2.4 m telescope (+YFOSC) of Yunnan Astronomical Observatories and the Xinglong 2.16 m telescope (+BFOSC) of the National Astronomical Observatories of China.

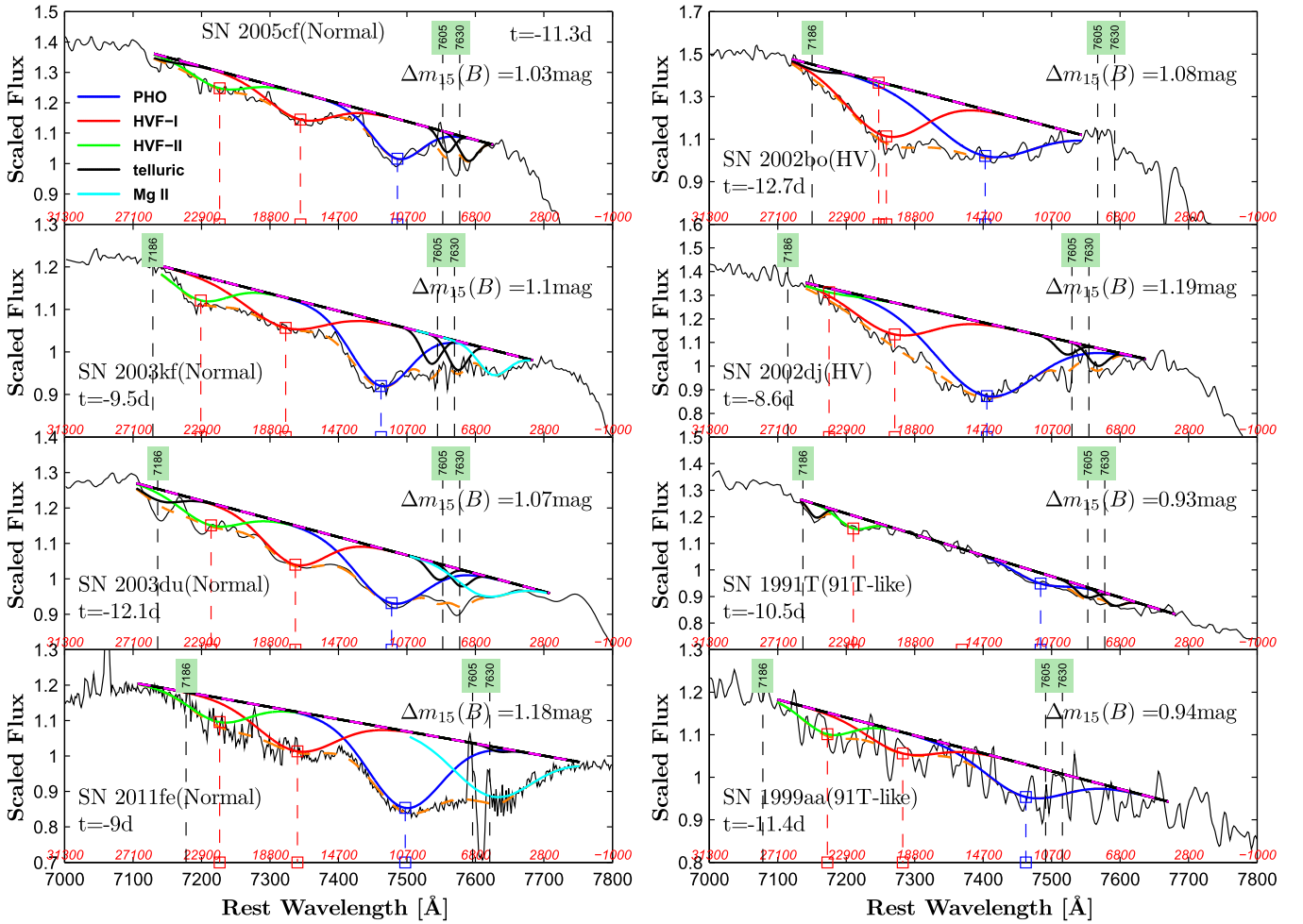


Figure 1. Absorption features of blueshifted O I $\lambda 7773$, centered near 7300–7500 Å in the optical spectrum, are shown for some representative SNe Ia. The SN name and the phase of the spectrum are shown in each panel. The left panels show the Normal SNe Ia in order of increasing strength (from top to bottom) for O I $\lambda 7773$ absorption, while the right panels show the HV and 91T/99aa-like SNe Ia. A multi-Gaussian fit is applied to determine different absorption components, with the blue curve representing the photospheric component, the red curve representing the main HVF (HVF-I), and the green curve representing the additional HVF at higher velocities (HVF-II). The orange curve represents the combined fits. The vertical dashed lines mark the positions of the absorption minima of the photospheric component and the two HVF components. The black dashed lines mark the positions of telluric absorptions (corrected for the redshifts of the SNe) at 7186, 7605, and 7630 Å. The number in brackets represents the B-band magnitude decline rate over the first 15 days after maximum light (see the text for references).

where subscripts $i = 1-6$ denote the photospheric component of O I $\lambda 7773$, the “main” HVF (hereafter HVF-I), the possible “second” HVF (hereafter HVF-II), and the telluric absorptions at 7168 Å, 7605 Å, and 7630 Å, respectively. In the above equation, A_i is the amplitude (i.e., the maximum absorption), σ_i is the dispersion (i.e., the standard deviation in a normal distribution), and λ_i^0 is the laboratory wavelength of a specific spectral line. Note that the positions of the telluric absorptions (and thereby the λ_i^0) are blueshifted relative to the rest-frame wavelengths because the spectrum was corrected for the redshift of the host galaxy.

In the fitting, the pseudo-continuum is defined as a straight line connecting the line wings on both sides of the absorption, and is determined through repeated visual inspections and careful manual adjustments in order to better counter the noise. As usual, the line strength of an absorption feature is quantified by the pseudo-equivalent width (pEW). From Equation (1), we have:

$$\text{pEW} = \sum \sqrt{2\pi} A_i \sigma_i \quad (2)$$

where the summation is performed for appropriate components.

Before fitting, we smoothed the observed spectrum around the O I $\lambda 7773$ absorption (i.e., covering the wavelength range from 7000 to 7800 Å) with a locally weighted scatter-plot smoothing method (Cleveland 1979) in order to reduce the effect of noise spikes on the fitting results, as the O I $\lambda 7773$ line (especially the HVF) is usually weak in early-time spectra of SNe Ia. In our previous work (Zhao et al. 2015), the photospheric velocity of Si II 5972 was used as an initial condition to constrain that of Si II $\lambda 6355$ because the HVF and photospheric component of the latter feature are often seriously blended. In determining the velocity of the O I $\lambda 7773$ line, however, we did not use the velocity condition from the Si II $\lambda 5972$ line or the Ca II NIR triplet lines because the HVF and photospheric component of the O I $\lambda 7773$ line are distinctly separated (i.e., by about 6000 km s⁻¹) and their locations can be better determined in early-time spectra, as shown in Figure 1. The only exceptions are for several HV SNe Ia where their HVFs and photospheric components show more severe blending (i.e., SN 2002dj) and the velocity of Si II $\lambda 5972$

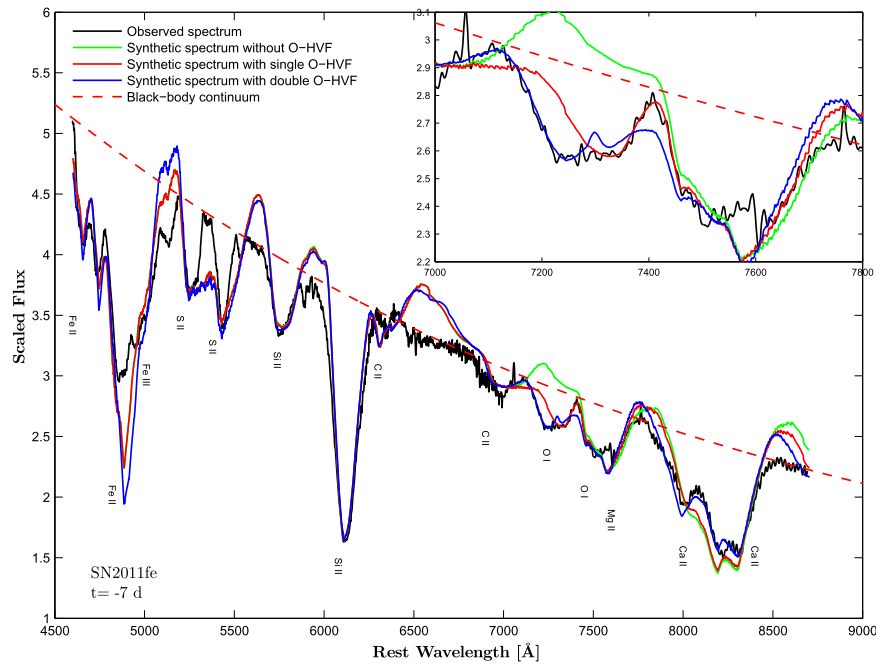


Figure 2. $t = -7$ day spectrum of SN 2011fe is compared with the synthetic spectrum from the SYNOW fit (Fisher et al. 1995). The green curve represents the synthetic spectrum without including the O-HVF; the red curve represents the fit with single O-HVF; the blue curve represents the fit with double O-HVFs at 18,000 km s^{-1} and 22,000 km s^{-1} , respectively.

is used to better locate the photospheric component of O I $\lambda 7773$.

As most of the published spectral data do not have accompanying flux errors, we adopt the R -squared statistic to fit the parameters of absorption features such as the amplitude A_i , the dispersion σ_i , and velocity of absorption minima v_i^0 . This fitting procedure is done through the Curve Fitting Toolbox in Matlab, where regression analysis can be conducted using the library of various models provided. Generally speaking, the fittings were well-performed and objectively determined by the absorption profiles, with the typical R -squared value being 0.97 for our sample. There are several reasons why the multi-Gaussian fitting applied in our analysis can be performed well without over/under-fitting. First, the blending between the HVF and photospheric component of O I $\lambda 7773$ is much weaker than that seen in Si II $\lambda 6355$ or the Ca II NIR triplet. Second, the contaminations from residual telluric absorptions are not very serious for our selected sample. For example, the blending ratio between the telluric absorption and the photospheric component of O I $\lambda 7773$ is overall small for our sample (see discussion below). Third, in most cases, the possible Mg II $\lambda 7890$ is not strong (with pEW $\lesssim 10$ Å) and it is well separated from the photospheric component of O I $\lambda 7773$.

Figure 1 shows the absorption features centering at O I $\lambda 7773$ in the $t \approx -10$ day spectra of some representative SNe Ia. A demonstration of applying the multi-Gaussian fit is shown in the plot, where the photospheric absorption of O I $\lambda 7773$ (at $\sim 12,000$ km s^{-1}) is accompanied by two additional absorptions on the blue side. These two absorptions can be attributed to the HVF-I and HVF-II of oxygen at velocities $\sim 18,000$ km s^{-1} and $\sim 22,000$ km s^{-1} , respectively, and this identification is secured by comparisons with the SYNOW fit as shown in Figure 2 (Fisher et al. 1995). We note that the different absorption components of the O I line are clearly separated from each other for Normal SNe Ia, while the O-HVF absorption tend to blend

with the photospheric component in some HV SNe Ia such as SN 2002bo and SN 2002dj.

In this work, errors of spectral fit were retrieved from the Matlab function “confint.” This function calculates the confidence bounds of the fitting results using $t\sqrt{((X^T X)^{-1} s^2)}$, where X is the Jacobian of fitted values, X^T is the transpose of X , s^2 is the mean squared error, and t is calculated using the inverse of Student’s cumulative distribution function. The errors of A_i and σ_i are then used to compute that of the pEW using Equation (2), and the error of λ_i is converted to that of the line velocity. Since the fitting is applied to the smoothed spectrum, the noise of the original spectrum is further factored into the above errors by taking the residual standard deviation between the original and smoothed data roughly as a 1σ error in the spectral fitting. The typical error from spectral noise is about 3% for our sample and the corresponding error in pEW is about 1.0 Å. An additional velocity error is also considered for the fits to the smoothed spectra, which is taken to be the velocity shift from the Gaussian fits to the smoothed and original spectra¹¹ or the standard error of these two fits (i.e., 460 km s^{-1} for the photospheric component and 515 km s^{-1} for the HVF for 87 spectra) when the Matlab code fails to fit the original spectra.

Moreover, the photospheric component of O I $\lambda 7773$ absorption might also be affected by the residual telluric absorptions. To obtain a quantitative estimation of this contamination, we introduce a parameter of blending ratio R_b , which measures the fraction that the line profile of the photospheric component of O I $\lambda 7773$ is overlapped by the telluric absorption. This ratio is calculated as $\text{pEW}_{\text{blending}}^{\text{telluric}}/\text{pEW}_{\text{PHO}}^{\text{O}}$, where $\text{pEW}_{\text{blending}}^{\text{telluric}}$

¹¹ The fit to the original spectra can be done for 87 spectra (out of 143) for our sample. The resultant velocities (and pEWs) are well consistent with those from fits to the smoothed spectra, with the adjusted R -squared coefficient for linear correlations being 0.91 for the photospheric component and 0.83 for the O-HVF component.

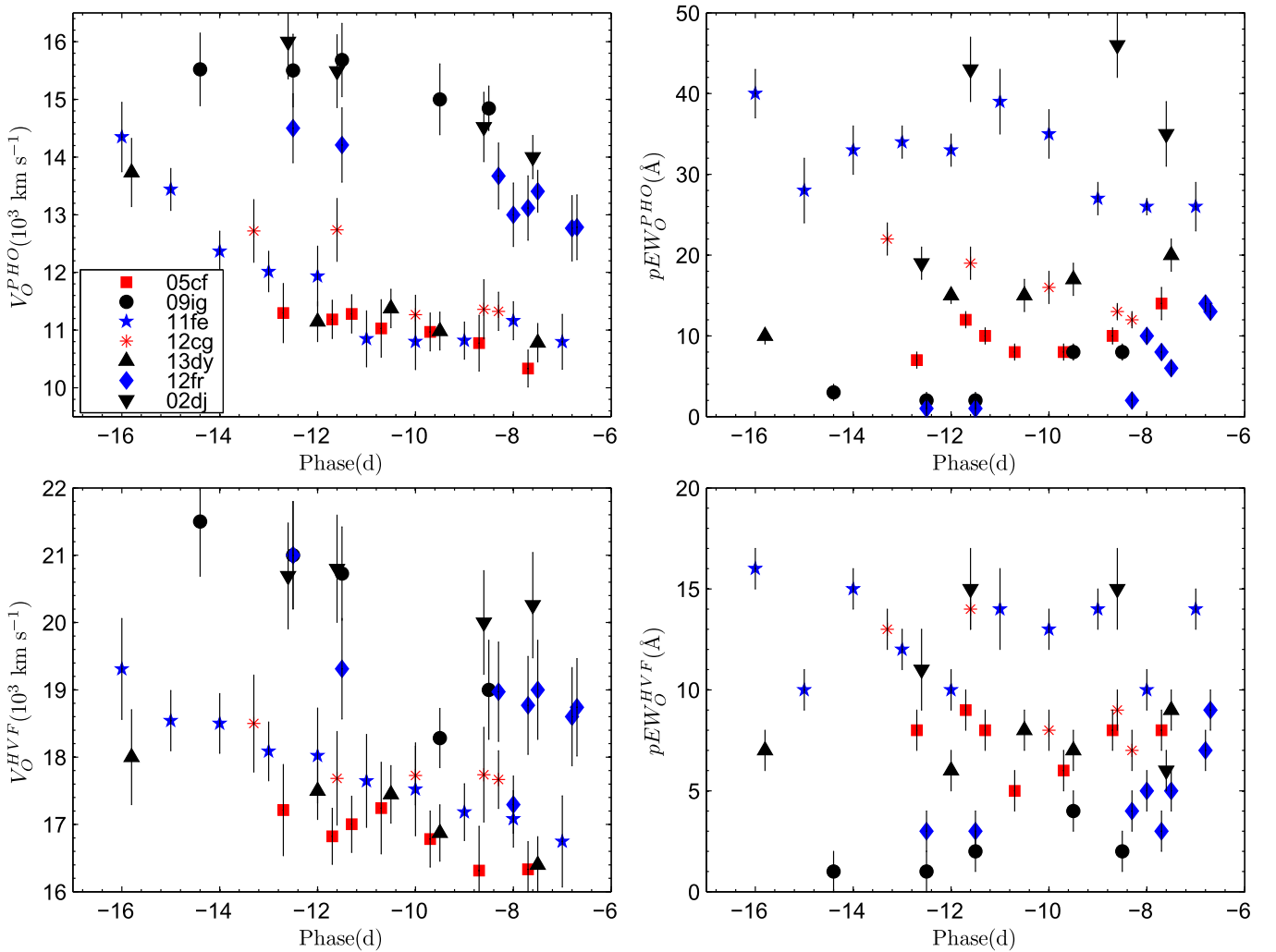


Figure 3. Left panels: evolution of the absorption strength of HVF and the photospheric component of O I $\lambda 7773$ for some well-observed SNe Ia such as SNe 2002dj, 2005cf, 2009ig, 2011fe, 2012cg, 2012fr, and 2013dy. Right panels: similar evolutions but for the absorption strength of the HVF and photospheric component of the O I line.

represents the pEW of the region of telluric feature that is blended with the photospheric component of O I $\lambda 7773$, and $\text{pEW}_{\text{PHO}}^{\text{O}}$ refers to the pEW of the O photospheric component. The results of this parameter measured for each spectrum of our sample are reported in the last column of Table 2. This blending ratio is, overall, small for our sample, with a mean value of only 3.7%, suggesting that the effect of residual telluric lines is negligible. In addition to the uncertainties listed above, the photospheric component of O I $\lambda 7773$ could also suffer from blending of an unknown component that could be due to Mg II $\lambda 7890$ or additional absorption feature of oxygen at lower velocities (i.e., $< 7000 \text{ km s}^{-1}$). However, these two effects are not considered in this work because they are difficult to quantify.

2.3. Temporal Evolution of O I $\lambda 7773$

The temporal evolution of the line velocity and strength of the O I $\lambda 7773$ absorption is shown in Figure 3 for some well-observed SNe Ia, including SNe 2002dj, 2005cf, 2009ig, 2011fe, 2012fr, and 2013dy (see Table 1 for references). According to the spectroscopic classification as proposed by Wang et al. (2009a), SN 2002dj and SN 2009ig belong to the HV subclass of SNe Ia, while SN 2005cf, SN 2011fe, and SN

2013dy can be put into the Normal subclass. SN 2012cg shares some properties with the SN 1999aa-like subclass, which is characterized by shallow silicon in the spectra (Silverman et al. 2012b; Zhang et al. 2014; Marion et al. 2015). SN 2012fr may lie at the boundary of the above classifications (Zhang et al. 2014).

As shown in the left panels of Figure 3, the O I $\lambda 7773$ absorptions of different SNe Ia show large differences in the velocity and the velocity evolution for both the HVF and photospheric component. For example, at $t \approx -10$ day, the photospheric velocity measured for our sample has a range from $\sim 11,000$ to $\sim 15,000 \text{ km s}^{-1}$, and the velocity of the HVF-I ranges from $\sim 17,000$ to $\sim 20,000 \text{ km s}^{-1}$. The O I lines (both the photospheric component and HVF-I) of HV SNe Ia have a velocity that is on average larger than that of the Normal SNe by $3000\text{--}4000 \text{ km s}^{-1}$ at comparable phases, similar to the case seen in Si II $\lambda 6355$ (Zhao et al. 2015). Restricting the data to the phases from $t \sim -13$ day to $t \sim -7$ day in the calculation of the velocity gradient, we find that the velocity gradients measured for the photospheric components of SN 2005cf, SN 2011fe, and SN 2013dy are -182 , -186 , and $-100 \text{ km s}^{-1}\text{day}^{-1}$, respectively, while the corresponding values obtained for their HVFs are -183 , -227 , and $-263 \text{ km s}^{-1}\text{day}^{-1}$. For SN 2002dj, SN 2009ig, SN

Table 1
Velocities and pEWs Near $t \sim -10$ day

SN	O I $\lambda 7773$							Si II $\lambda 6355$				Ca II NIR				v_0^{SiP} (km s $^{-1}$)	$\Delta m_{15}(\text{B})^{\text{q}}$ (mag)	Ref. ^r
	t^{a} (day)	V_{P}^{b} (km s $^{-1}$)	W_{P}^{c} (\AA)	V_{H}^{d} (km s $^{-1}$)	W_{H}^{e} (\AA)	V_{S}^{f} (km s $^{-1}$)	W_{S}^{g} (\AA)	V_{P}^{h} (km s $^{-1}$)	W_{P}^{i} (\AA)	V_{H}^{j} (km s $^{-1}$)	W_{H}^{k} (\AA)	V_{P}^{l} (km s $^{-1}$)	W_{P}^{m} (\AA)	V_{H}^{n} (km s $^{-1}$)	W_{H}^{o} (\AA)			
1991M	-7.8	12501 (562)	40(4)	17000 (675)	27(2)	22969 (841)	3(1)	13384 (624)	118(10)	18000 (766)	1(1)	14672 (345)	129(16)	23788 (495)	96(6)	12511 (434)	1.51(10)	A; B;1
1991T*	-10.5	11362 (331)	4(1)	16000 (643)	1(1)	22539 (504)	2(1)	12500 (582)	17(2)	17000 (735)	1(1)	9509 (476)	0.93(05)	A;B;2
1994D	-9.5	12601 (542)	22(2)	17631 (697)	10(1)	21679 (822)	5(1)	12249 (578)	81(6)	18900 (788)	21(1)	12322 (322)	48(5)	23177 (491)	75(7)	11021 (330)	1.37(03)	A;B;3
1997bq	-11.8	13390 (302)	34(3)	18197 (412)	28(4)	22603 (491)	14(2)	16545 (722)	133(10)	21654 (878)	37(3)	15500 (605)	59(5)	24000 (863)	236(24)	13000 (650)	1.01(05)	A;4
1998dm	-10.9	11702 (338)	21(2)	17709 (429)	8(1)	22237 (501)	5(1)	11715 (356)	65(4)	18011 (516)	13(1)	12179 (319)	69(6)	22314 (475)	91(5)	11058 (553)	0.85(05)	A;B;4;5
1998ef	-8.9	11222 (509)	29(4)	16333 (664)	50(5)	21660 (831)	14(1)	14394 (634)	150(12)	18000 (748)	1(1)	11778 (314)	118(12)	21011 (457)	116(12)	13260 (384)	1.30(05)	A; B;4;5
1999aa*	-11.4	12216 (539)	11(1)	19535 (750)	6(1)	24103 (889)	4(1)	12457 (590)	40(4)	18869 (791)	1(1)	10484 (310)	0.94(01)	A;B;4;5
1999dk	-7.7	13531 (460)	32(2)	18664 (651)	22(4)	23000 (856)	1(1)	13818 (637)	116(9)	18214 (772)	18(2)	14104 (352)	108(9)	22725 (484)	99(5)	12500 (625)	1.15(04)	B;5
1999dq*	-9.6	12355 (531)	5(1)	18051 (699)	5(1)	23586 (866)	5(1)	11156 (552)	27(2)	18875 (798)	4(1)	10939 (314)	0.96(04)	A;4;5
1999ee	-9.4	13000 (383)	5(1)	18000 (706)	6(1)	23088 (509)	5(1)	10800 (544)	30(2)	17694 (490)	54(3)	10189 (332)	0.96(05)	A; B;6
2000dx ⁺	-9.0	12501 (349)	18(1)	17715 (431)	11(1)	22738 (507)	7(1)	13793 (414)	121(6)	19504 (520)	27(3)	12500 (625)	...	B;
2000fa	-9.1	12011 (524)	20(2)	20342 (779)	10(1)	26000 (948)	1(1)	13391 (624)	85(7)	20756 (851)	18(2)	12863 (330)	47(5)	23994 (862)	129(13)	12106 (344)	0.91(04)	A;B;4;5
2001el ⁺	-9.0	11701 (347)	12(1)	17847 (437)	8(1)	22760 (506)	4(1)	13428 (368)	84(3)	20088 (511)	39(5)	14003 (338)	68(7)	24553 (499)	223(21)	11715 (346)	1.16(03)	7;8
2002cr	-7.6	9371 (439)	39(3)	16117 (644)	16(2)	20926 (792)	2(1)	10929 (328)	106(8)	16128 (466)	3(1)	10017 (292)	1.23(04)	A; B;5
2002cs ⁺	-9.0	14465 (383)	37(4)	19000 (736)	24(2)	23782 (523)	11(2)	14816 (446)	109(9)	19197 (516)	23(1)	13911 (346)	97(5)	21900 (799)	24(3)	13982 (700)	1.03(05)	A;B;4
2002dj	-8.6	14521 (602)	46(4)	20000 (771)	15(2)	24000 (887)	1(1)	15108 (677)	145(11)	21344 (868)	19(2)	14222 (351)	118(11)	23862 (500)	161(9)	13095 (655)	1.19(05)	A;B;5;9
2002er	-8.9	12962 (355)	35(4)	19454 (465)	15(2)	23047 (512)	20(2)	14390 (654)	103(8)	19900 (824)	1(1)	11895 (346)	1.23(03)	A;B;5
2003U	-8.8	13054 (555)	51(7)	17403 (738)	21(2)	24105 (891)	1(1)	12985 (388)	121(11)	18000 (766)	2(1)	11046 (342)	1.46(10)	A;B;9
2003cg	-8.4	11559 (342)	21(2)	16576 (420)	12(1)	21848 (494)	5(1)	11603 (350)	89(9)	18300 (765)	3(1)	12000 (497)	79(8)	21890 (471)	25(3)	11322 (326)	1.22(10)	A;5;9
2003du	-12.1	11762 (336)	16(2)	17250 (424)	10(1)	22363 (502)	6(1)	12000 (581)	74(6)	18344 (774)	23(2)	11466 (304)	69(6)	21957 (470)	165(16)	10557 (306)	1.07(06)	A;B;5;9

Table 1
(Continued)

SN	O I $\lambda 7773$							Si II $\lambda 6355$				Ca II NIR				v_0^{SiP} (km s $^{-1}$)	$\Delta m_{15(B)}$ ^q (mag)	Ref. ^r
	t^a (day)	V_P^b (km s $^{-1}$)	W_P^c (\AA)	V_H^d (km s $^{-1}$)	W_H^e (\AA)	V_S^f (km s $^{-1}$)	W_S^g (\AA)	V_P^h (km s $^{-1}$)	W_P^i (\AA)	V_H^j (km s $^{-1}$)	W_H^k (\AA)	V_P^l (km s $^{-1}$)	W_P^m (\AA)	V_H^n (km s $^{-1}$)	W_H^o (\AA)			
2003ek ⁺	-10.0	12483 (536)	38(4)	20853 (794)	23(3)	26000 (948)	22(2)	11042 (330)	96(5)	18082 (771)	1(1)	10832 (320)	...	A;B;
2003fa [*]	-9.2	10938 (488)	11(1)	18500 (719)	4(1)	22412 (838)	4(1)	11369 (336)	37(2)	19497 (513)	5(1)	10357 (518)	0.96(03)	A;B;5;9
2003kc	-11.4	13563 (573)	37(4)	18611 (725)	31(3)	21409 (807)	3(1)	15646 (694)	152(16)	18000 (767)	1(1)	12723 (608)	1.19(03)	A;B;9
2003kf	-9.5	12240 (535)	15(1)	17860 (710)	9(1)	23000 (856)	5(1)	11998 (358)	75(4)	18200 (771)	12(2)	12340 (323)	45(4)	23590 (496)	82(7)	11444 (573)	1.10(05)	A;B;1
2004dt	-10.8	12157 (335)	43(2)	17362 (418)	64(7)	21983 (494)	28(3)	15000 (750)	137(14)	20162 (1009)	30(3)	12500 (512)	58(6)	21300 (780)	79(5)	14110 (406)	1.14(04)	A;B; C;5;10
2004eo	-11.4	12500 (528)	21(3)	17500 (423)	11(2)	24479 (502)	1(1)	11684 (364)	124(10)	18000 (774)	1(1)	11800 (482)	144(13)	20634 (445)	155(8)	10497 (296)	1.38(03)	A;B;C; 5;10
2004ey	-8.2	12114 (523)	18(2)	17930 (698)	13(1)	23000 (856)	2(1)	11759 (352)	88(5)	20188 (532)	6(1)	11474 (308)	59(5)	22386 (477)	81(7)	11220 (324)	0.96(06)	B; C;5;10
2005cf	-10.2	10999 (414)	8(1)	17012 (549)	6(1)	22700 (678)	3(1)	11773 (348)	83(4)	18674 (503)	45(3)	12963 (520)	69(7)	23406 (492)	243(25)	10276 (302)	1.03(01)	A;B;11
2005cg ⁺	-9.0	11555 (509)	15(2)	18000 (704)	5(1)	22210 (831)	2(1)	12137 (366)	49(3)	18661 (806)	30(2)	9906 (283)	32(2)	23239 (489)	115(11)	11590 (342)	...	A;
2005el	-8.1	11000 (460)	31(2)	17078 (416)	14(2)	22511 (503)	4(1)	11355 (338)	76(5)	18799 (857)	3(1)	11357 (304)	58(6)	21059 (454)	46(3)	10811 (304)	1.31(06)	A;B; C;5;9;10
2005eu [*]	-9.1	12447 (535)	5(1)	18782 (728)	2(1)	23200 (862)	4(1)	11161 (324)	42(2)	18300 (774)	1(1)	11068 (554)	0.94(04)	A; B;5;9
2006X	-11.1	15500 (660)	5(1)	21000 (798)	24(3)	24040 (527)	7(1)	16357 (818)	121(13)	22500 (1125)	73(8)	15577 (441)	1.17(05)	A; B;C;12
2006ax ⁺	-10.6	11061 (490)	24(2)	16651 (662)	10(2)	22137 (832)	2(1)	12105 (361)	94(5)	18281 (774)	4(1)	11554 (311)	85(9)	20324 (446)	108(6)	10503 (298)	1.02(02)	A;B;C; 9;10
2006dd	-12.4	11156 (341)	21(2)	17280 (427)	12(2)	22309 (502)	6(1)	11306 (340)	88(5)	18000 (765)	1(1)	10500 (525)	1.07(03)	C;13
2006dm	-7.9	10000 (460)	55(6)	16351 (653)	23(3)	21000 (795)	7(1)	12454 (372)	110(6)	18000 (765)	1(1)	11800 (590)	1.53(06)	B;5
2006dy	-11.8	10556 (491)	38(4)	18317 (722)	8(1)	22949 (842)	2(1)	12363 (370)	110(5)	20000 (827)	10(1)	10459 (523)	...	B;
2006gr	-9.2	13100 (556)	8(1)	19269 (744)	7(1)	23148 (860)	3(1)	13752 (418)	55(3)	20465 (533)	32(3)	10723 (299)	30(3)	23385 (492)	129(13)	11492 (366)	1.03(06)	A;B;5;9
2006kf	-8.3	11991 (460)	64(4)	17418 (673)	21(3)	22152 (830)	6(1)	12953 (390)	128(7)	19239 (518)	4(1)	11378 (322)	1.48(01)	A;B;C; 9;13
2006le	-8.9	12209 (524)	9(1)	18176 (709)	7(1)	23003 (855)	4(1)	12882 (576)	68(5)	20115 (806)	25(4)	11159 (325)	12(2)	24000 (862)	151(13)	11005 (342)	0.89(05)	A;B;5;9
2007F [*]	-9.7	11868 (518)	6(1)	17995 (702)	2(1)	22964 (843)	2(1)	12055 (348)	71(5)	20372 (513)	10(2)	10617 (296)	41(4)	24000 (861)	106(9)	11254 (324)	1.03(01)	A;B;9

Table 1
(Continued)

SN	O I $\lambda 7773$							Si II $\lambda 6355$				Ca II NIR				v_0^{SiP} (km s $^{-1}$)	$\Delta m_{15(B)}$ ^q (mag)	Ref. ^r
	t^a (day)	V_P^b (km s $^{-1}$)	W_P^c (\AA)	V_H^d (km s $^{-1}$)	W_H^e (\AA)	V_S^f (km s $^{-1}$)	W_S^g (\AA)	V_P^h (km s $^{-1}$)	W_P^i (\AA)	V_H^j (km s $^{-1}$)	W_H^k (\AA)	V_P^l (km s $^{-1}$)	W_P^m (\AA)	V_H^n (km s $^{-1}$)	W_H^o (\AA)			
2007af	-11.3	11183 (496)	35(3)	17000 (674)	19(2)	22091 (829)	1(1)	12629 (632)	113(12)	18300 (915)	1(1)	11647 (318)	93(10)	20725 (454)	151(9)	11007 (315)	1.20(05)	A; B;C;5;9
2007bd	-8.1	11580 (508)	39(4)	17500 (689)	20(2)	24000 (887)	1(1)	13709 (402)	130(6)	18300 (775)	1(1)	12459 (324)	93(10)	21064 (457)	71(4)	12557 (366)	1.24(01)	A;B;C;9
2007bm	-8.2	11246 (507)	36(2)	17170 (676)	12(1)	21473 (813)	5(1)	11145 (334)	89(4)	18300 (774)	1(1)	11064 (301)	85(7)	20297 (444)	41(2)	10500 (525)	1.19(02)	A;B;C;9
2007ca	-10.4	11000 (491)	17(2)	17811 (700)	8(1)	23102 (859)	1(1)	12053 (362)	67(4)	18564 (786)	10(1)	11230 (314)	1.10(01)	A; B;C;5;9
2007le	-9.7	14623 (603)	9(1)	20142 (776)	4(1)	24000 (887)	2(1)	13795 (637)	99(8)	21000 (858)	54(4)	14500 (349)	55(6)	26710 (544)	288(29)	12410 (370)	1.01(05)	A;B; C;5
2008ar	-9.1	12207 (529)	13(1)	17145 (674)	7(1)	21673 (819)	3(1)	12187 (336)	93(4)	19000 (492)	37(5)	13247 (312)	58(5)	23921 (681)	185(13)	10634 (316)	1.08(06)	A;B;C; 5;14
2008bc	-9.7	14337 (606)	15(2)	19000 (736)	6(1)	23364 (865)	5(1)	12933 (612)	90(6)	19609 (815)	38(3)	11774 (327)	41(3)	24000 (862)	253(11)	11600 (580)	0.93(01)	C;13
2008bf	-9.5	12000 (522)	14(2)	18677 (723)	5(1)	24010 (886)	2(1)	12153 (360)	61(5)	19023 (512)	20(1)	12412 (319)	50(5)	22942 (486)	101(10)	11466 (336)	1.03(07)	A;B; C;5;9
2008hv	-11.3	14314 (375)	36(3)	18500 (721)	9(1)	22505 (503)	2(1)	13735 (424)	105(6)	19241 (518)	41(3)	14062 (347)	95(9)	24000 (863)	257(27)	10926 (312)	1.25(01)	B;C;14
2009aa	-8.7	10381 (481)	28(2)	16824 (683)	13(1)	22255 (829)	1(1)	10513 (316)	80(4)	18300 (774)	1(1)	10516 (294)	85(7)	20889 (454)	23(2)	10000 (500)	1.12(05)	C;13
2009ab	-10.8	11303 (335)	30(2)	17730 (428)	16(2)	23107 (512)	5(1)	10921 (547)	73(8)	18300 (915)	1(1)	10839 (306)	1.21(10)	C;13
2009ig	-9.5	15000 (614)	8(1)	18284 (440)	4(1)	22689 (506)	6(1)	14896 (668)	84(6)	22700 (906)	12(1)	13400 (670)	0.89(02)	B;15;16
2011by	-12.4	11418 (333)	30(2)	18592 (443)	10(1)	23001 (511)	1(1)	12209 (368)	86(4)	18300 (774)	7(1)	12000 (497)	116(12)	20650 (450)	79(5)	10300 (515)	1.14(03)	D;17
2011df ⁺	-9.0	13711 (574)	9(1)	18615 (722)	6(1)	21961 (825)	3(1)	12280 (366)	96(5)	19500 (811)	29(2)	11005 (348)	...	D;
2011fe ⁺	-10.0	10819 (485)	35(3)	17522 (689)	14(1)	22379 (837)	3(1)	11917 (569)	99(9)	20300 (835)	3(1)	11537 (296)	108(9)	19939 (431)	64(4)	10444 (529)	1.18(03)	D;17;18
2012cg ⁺	-10.0	11266 (338)	16(2)	17726 (436)	8(1)	23564 (517)	2(1)	12278 (587)	64(5)	18936 (790)	31(3)	13052 (334)	78(7)	21722 (466)	98(5)	10000 (500)	0.83(05)	D;19;20
2012et ⁺	-8.0	13550 (525)	27(3)	18500 (720)	11(2)	23043 (948)	9(1)	14051 (645)	119(9)	18421 (779)	14(1)	13053 (408)	1.24(04)	D;
2012fr ⁺	-11.5	14208 (645)	1(1)	19312 (747)	3(1)	26000 (948)	2(1)	13400 (576)	40(1)	22507 (857)	109(10)	13000 (528)	9(1)	27000 (547)	150(14)	12200 (611)	0.80(01)	D;21
2013dy ⁺⁺	-10.0	11179 (331)	16(2)	17160 (423)	8(1)	23184 (515)	6(1)	11404 (562)	49(4)	18417 (777)	5(1)	10644 (435)	58(6)	21985 (464)	52(4)	10300 (515)	0.92(01)	D;22;23
2013gs ⁺	-9.7	13748 (573)	10(1)	19451 (741)	5(1)	25227 (928)	1(1)	12873 (608)	67(5)	17561 (752)	56(4)	9756 (405)	61(7)	21112 (453)	185(20)	12200 (610)	1.05(01)	D;

Table 1
(Continued)

SN	O I $\lambda 7773$							Si II $\lambda 6355$				Ca II NIR				v_0^{SiP} (km s ⁻¹)	$\Delta m_{15}(\text{B})^{\text{q}}$ (mag)	Ref. ^r
	t^{a} (day)	V_{P}^{b} (km s ⁻¹)	W_{P}^{c} (Å)	V_{H}^{d} (km s ⁻¹)	W_{H}^{e} (Å)	V_{S}^{f} (km s ⁻¹)	W_{S}^{g} (Å)	V_{P}^{h} (km s ⁻¹)	W_{P}^{i} (Å)	V_{H}^{j} (km s ⁻¹)	W_{H}^{k} (Å)	V_{P}^{l} (km s ⁻¹)	W_{P}^{m} (Å)	V_{H}^{n} (km s ⁻¹)	W_{H}^{o} (Å)			
2013gy	-9.1	12106 (538)	32(4)	16553 (710)	17(2)	21000 (911)	3(1)	13211 (392)	121(6)	18300 (775)	1(1)	12500 (512)	158(16)	20423 (447)	121(7)	11000 (316)	1.20(01)	D;
2014J ⁺	-10.5	14438 (607)	19(2)	19972 (775)	7(1)	23500 (872)	3(1)	13920 (632)	114(9)	20322 (816)	25(2)	13043 (439)	52(5)	24651 (693)	190(19)	12050 (360)	1.02(01)	D;

Notes. Spectral parameters measured for O I $\lambda 7773$, Si II $\lambda 6355$, and the Ca II NIR triplet in the $t \sim -10 \pm 2.5$ day spectra of SNe Ia. Note that the velocity, pEW, photospheric component, HVF-I, and HVF-II are abbreviated to V, W, P, H, and S, respectively. The “***” and “*+” after the SN names denote the 99aa-like and 91T-like SNe Ia, respectively, while the “+” marks the SNe whose spectra used for the measurements of the Ca II NIR triplet and Si II $\lambda 6355$ (or O I $\lambda 7773$) are taken at slightly different epochs. The 1σ uncertainties shown in the brackets are in units of 1 km s⁻¹ for velocity, 1 Å for equivalent width, and 0.01 mag for $\Delta m_{15}(\text{B})$, respectively.

References. A—CfA Supernova Program (Matheson et al. 2008; Blondin et al. 2012); B—Berkeley Supernova Program (Silverman et al. 2012a); C—CSP (Folatelli et al. 2013); D—Tsinghua Supernova Program; 1—(Hachinger et al. 2006); 2—(Lira et al. 1998); 3—(Patat et al. 1996); 4—(Jha et al. 2006); 5—(Ganeshalingam et al. 2010); 6—(Stritzinger et al. 2002); 7—(Krisciunas et al. 2003); 8—(Mattila et al. 2005); 9—(Hicken et al. 2009); 10—(Contreras et al. 2010); 11—(Wang et al. 2009a); 12—(Wang et al. 2008); 13—(Stritzinger et al. 2011); 14—(Hicken et al. 2012); 15—(Marion et al. 2013); 16—(Foley et al. 2012); 17—(Graham et al. 2015); 18—(Zhang et al. 2016); 19—(Marion et al. 2016); 20—(Silverman et al. 2012b); 21—(Zhang et al. 2014); 22—(Zheng et al. 2013); 23—(Zhai et al. 2016).

^a Days since B-band maximum light.

^b Velocity of O I $\lambda 7773$ for the photospheric component.

^c pEW of O I $\lambda 7773$ for the photospheric component.

^d Velocity of O I $\lambda 7773$ for the HVF-I component.

^e pEW of O I $\lambda 7773$ for the HVF-I component.

^f Velocity of O I $\lambda 7773$ for the HVF-II component.

^g pEW of O I $\lambda 7773$ for the HVF-II component.

^h Velocity of Si II $\lambda 6355$ for the photospheric component.

ⁱ pEW of Si II $\lambda 6355$ for the photospheric component.

^j Velocity of Si II $\lambda 6355$ for the HVF component.

^k pEW of Si II $\lambda 6355$ for the HVF component.

^l Velocity of the Ca II IR triplet for the photospheric component.

^m pEW of the Ca II IR triplet for the photospheric component.

ⁿ Velocity of the Ca II IR triplet for the HVF component.

^o pEW of the Ca II IR triplet for the HVF component.

^p Velocity of Si II $\lambda 6355$ measured near maximum light.

^q Light-curve parameter, B-band light-curve decline rate $\Delta m_{15}(\text{B})$.

^r References for both spectra and photometry.

2012cg, and SN 2012fr, the velocity gradients of the photospheric components are -379 , -199 , -329 , and -257 $\text{km s}^{-1}\text{day}^{-1}$, while the corresponding values for the HVFs are -134 , -644 , -136 , and -413 $\text{km s}^{-1}\text{day}^{-1}$. The Normal SNe Ia appear to have a relatively uniform velocity evolution compared to other subclasses of SNe Ia. This may enable better extrapolations of absorption velocity to the value at a given phase (i.e., $t \sim -10$ day) for some normal sample when necessary. In contrast, the velocity evolution of SN 2002dj and SN 2009ig shows large scatter for either the HVFs or the photospheric components. This may be caused, to some extent, by the HV SNe Ia suffering more serious line blending and it thus being more difficult to separate the HVFs from the photospheric components.

The strength of the $\text{O I } \lambda 7773$ absorption is plotted as a function of phase in the right panels of Figure 3, which shows even larger scatter than the velocity. One can see that the O I absorptions are found to be strong in some SNe Ia such as SN 2002dj and SN 2011fe, but they are marginally detected in other objects such as SN 2009ig and SN 2012fr. Note, however, that the absorption strength of the O-HVF does not show significant variation with time for our sample, in particular the Normal subsample. This is different from the trend seen in the HVFs of the $\text{Si II } \lambda 6355$ line and the Ca II NIR triplet, which become weaker at a faster rate, perhaps due to having an optically thin environment in their outermost layers (see the references in Zhao et al. 2015).

3. STATISTICAL ANALYSIS

Table 1 lists the line velocities and strengths of $\text{O I } \lambda 7773$, $\text{Si II } \lambda 6355$, the Ca II NIR triplet, and $\text{C II } \lambda 6580$ absorptions obtained at $t \sim -10$ day for 62 SNe Ia. If more than one spectrum is available during the period from $t = -11$ day to $t = -9$ day the median values are presented. The B-band light-curve decline rate $\Delta m_{15}(\text{B})$ (Phillips 1993) is also listed. The detailed results for the measurements of the velocities and pEWs of the $\text{O I } \lambda 7773$ and $\text{C II } \lambda 6580$ absorptions at different phases are tabulated in Tables 2 and 3. Given the uncertainties due to line blending and/or the intrinsically larger scatter in the temporal evolution of O I absorption for HV SNe Ia, we concentrate on the spectroscopically normal SNe Ia with $v_0^{\text{Si}} < 12,500$ km s^{-1} in the following analysis.

3.1. Expansion Velocity from $\text{O I } \lambda 7773$

The velocity distribution of the ejected matter at different layers of the exploding WD can provide strong constraints on its compositional structure. To obtain an overall picture of the velocity distributions of $\text{C II } \lambda 6580$, $\text{Si II } \lambda 6355$, $\text{O I } \lambda 7773$, and the Ca II NIR triplet, we construct the mean spectrum using the spectra of a subsample of Normal SNe Ia whose spectra have a sufficiently high signal-to-noise ratio (S/N) (i.e., $\text{S/N} \gtrsim 20$) and cover phases close to $t = -10$ day. The mean profiles of the above four absorption features are shown in Figure 4, where the Ca II lines are characterized by prominent HVFs at $\sim 22,000$ km s^{-1} and the O I line is characterized by the HVF-I at $\sim 18,000$ km s^{-1} and a possible HVF-II at $\sim 22,000$ km s^{-1} . The small notch on the blue side of the $\text{Si II } \lambda 6355$ absorption corresponds to the HVF of Si formed at a velocity of about $18,000$ km s^{-1} . The $\text{C II } \lambda 6580$ absorption does not show any significant signature of an absorption feature at higher velocities. As can be seen, the photospheric components of different species have similar velocities (see the blue dashed

line in Figure 4). Note that Figure 4 is constructed for illustrative purpose only.

Figure 5 shows the expansion velocities measured from absorption minima of Si II , Ca II , and C II lines versus that from the O I line. At the photospheric layer, the velocity of the O I line shows a positive correlation with those of the Si II , Ca II , and C II lines; and a linear fit indicates that the O I velocity is slightly lower than the Si II and C II velocities by about 750 km s^{-1} . At the outer layers, the HVF-I of O (O-HVF-I) shows a similar but slightly lower central velocity compared to the Si-HVF; and at the outermost layers, the HVF-II of O has a velocity that is roughly comparable to the Ca-HVFs. This similarity in expansion velocities indicates that the fuel-indicative O and the burned Si (or Ca) are physically connected. The observation results for the small velocity differences between the lines, and the fact that the Ca-HVFs have higher velocities relative to the Si-HVFs, might be well explained by different ionization (or excitation) energies being required to produce the lines of $\text{O I } \lambda 7773$ (i.e., $E_{\text{ex}} = 9.15$ eV), $\text{Si II } \lambda 6355$ (i.e., $E_{\text{ex}} = 8.12$ eV), and the Ca II NIR triplet (i.e., $E_{\text{ex}} = 1.7$ eV). For the relatively low temperature expected for the outermost HVF forming layer, the Ca II NIR triplet is more easily formed and saturated compared to the Si II and O I lines.

3.2. Equivalent Width of $\text{O I } \lambda 7773$

The line strength of $\text{O I } \lambda 7773$ absorption carries important information on the diversity of SNe Ia. Figures 6 shows the pEW (for the photospheric component and HVF) of O I absorption versus the corresponding velocities, measured from the $t \approx -10$ day spectra of our SN Ia sample. As can be readily seen in these figures, these two quantities do not show significant correlation for the full sample, as indicated by the lower Pearson coefficients. Excluding the HV SNe Ia from the statistical sample, a modest anti-correlation seems to emerge between the pEWs and velocities of O I lines, although there are a few outliers. These results indicate that a smaller amount of oxygen is detected in SNe Ia with relatively larger expansion velocities. Such an inverse relation becomes stronger for the subsample with prominent detection of $\text{C II } \lambda 6580$ absorption, i.e., $\text{pEW} \gtrsim 1.0$ Å at $t \approx -10$ day (see Table 3 for the detailed results of the measurements). The corresponding Pearson coefficients, ρ , are -0.64 and -0.67 for the correlations of the HVFs and photospheric components, respectively. The much tighter pEW–velocity relation for $\text{O I } \lambda 7773$ absorption suggests that the SNe Ia showing prominent carbon in their spectra may form a distinct population with relatively smaller diversity.

We notice that the velocity–pEW correlation seen in $\text{O I } \lambda 7773$ absorption is the opposite to that seen in the $\text{Si II } \lambda 6355$ line (Wang et al. 2009a; Blondin et al. 2012), which directly reflects the different roles that O and Si play in burning in the HVF and photospheric layers. In the right-most panel of Figure 6, we further examine the relation between the absorption strengths of the HVF and the photospheric component of $\text{O I } \lambda 7773$. We find that the pEW of the O-HVF absorption is highly correlated with that of the O photospheric absorption, which has a Pearson coefficient of 0.86 . This strong correlation indicates that the O detected at the outermost layers of the ejecta is intrinsic to the SNe, rather than coming from other sources such as CSM, which usually lies far outside the exploding WD and should not have such a strong connection with the photosphere unless CSM properties are

Table 2
Fit Results of O I $\lambda 7773$

SN	t^a (day)	V_p^b (km s $^{-1}$)	W_p^c (\AA)	V_H^d (km s $^{-1}$)	W_H^e (\AA)	V_S^f (km s $^{-1}$)	W_S^g (\AA)	R_b^h
1990N	-13.9	12851(353)	11(2)	17946(419)	12(1)	21349(795)	10(2)	0
1991M	-7.8	12501(562)	40(4)	17000(675)	27(2)	22969(841)	3(1)	0.13
1991T	-10.5	11362(331)	4(1)	16000(643)	1(1)	22539(504)	2(1)	0.06
1994D	-11.1	13119(361)	15(2)	18625(444)	10(1)	21719(486)	2(1)	0
1994D	-9.5	12601(542)	22(2)	17631(697)	10(1)	21679(822)	5(1)	0
1994D	-8.5	12001(507)	26(2)	17785(675)	10(1)	22284(816)	1(1)	0
1997bq	-11.8	13390(302)	34(3)	18197(412)	28(4)	22603(491)	14(2)	0.14
1998dk	-7.1	14496(387)	23(3)	20364(479)	15(2)	23790(527)	3(1)	0.07
1998dm	-10.9	11702(338)	21(2)	17709(429)	8(1)	22237(501)	5(1)	0.08
1998ef	-8.9	11222(509)	29(4)	16333(664)	50(5)	21660(831)	14(1)	0
1999aa	-11.4	12216(539)	11(1)	19535(750)	6(1)	24103(889)	4(1)	0
1999dk	-7.7	13531(460)	32(2)	18664(651)	22(4)	23000(856)	1(1)	0.05
1999dq	-9.6	12355(531)	5(1)	18051(699)	5(1)	23586(866)	5(1)	0
1999ee	-9.4	13000(383)	5(1)	18000(706)	6(1)	23088(509)	5(1)	0.08
1999ee	-7.4	13000(378)	8(1)	18000(705)	7(1)	23025(510)	6(1)	0.12
2000dx	-9	12501(349)	18(1)	17715(431)	11(1)	22738(507)	7(1)	0
2000fa	-9.1	12011(524)	20(2)	20342(779)	10(1)	26000(948)	1(1)	0
2001el	-9	11701(347)	12(1)	17847(437)	8(1)	22760(506)	4(1)	0.09
2002bo	-12.7	14626(603)	31(3)	20507(782)	26(2)	21000(795)	1(1)	0
2002cr	-7.6	9371(439)	39(3)	16117(644)	16(2)	20926(792)	2(1)	0
2002cs	-9	14465(383)	37(4)	19000(736)	24(2)	23782(523)	11(2)	0.02
2002dj	-12.6	16000(645)	19(2)	20693(787)	11(2)	24000(887)	1(1)	0
2002dj	-11.6	15487(632)	43(4)	20799(797)	15(2)	24000(887)	1(1)	0
2002dj	-8.6	14521(602)	46(4)	20000(771)	15(2)	24000(887)	1(1)	0.06
2002dj	-7.6	14000(375)	35(4)	20258(782)	6(1)	24000(887)	2(1)	0.1
2002er	-8.9	12962(355)	35(4)	19454(465)	15(2)	23047(512)	20(2)	0.15
2002er	-7.9	13183(363)	36(3)	20520(596)	15(2)	24000(887)	8(1)	0.09
2003U	-8.8	13054(555)	51(7)	17403(738)	21(2)	24105(891)	1(1)	0
2003cg	-8.4	11559(342)	21(2)	16576(420)	12(1)	21848(494)	5(1)	0.11
2003cg	-7.4	11763(515)	22(2)	16100(647)	8(1)	22572(843)	1(1)	0.08
2003du	-12.1	11762(336)	16(2)	17250(424)	10(1)	22363(502)	6(1)	0.12
2003ek	-10	12483(536)	38(4)	20853(794)	23(3)	26000(948)	22(2)	0
2003fa	-9.2	10938(488)	11(1)	18500(719)	4(1)	22412(838)	4(1)	0
2003fa	-8.8	11009(489)	9(1)	18500(719)	4(1)	22230(833)	3(1)	0
2003kc	-11.4	13563(573)	37(4)	18611(725)	31(3)	21409(807)	3(1)	0
2003kf	-9.5	12240(535)	15(1)	17860(710)	9(1)	23000(856)	5(1)	0.09
2003kf	-8.8	12222(534)	16(2)	17651(702)	9(1)	23000(856)	4(1)	0.08
2004dt	-10.8	12157(335)	43(2)	17362(418)	64(7)	21983(494)	28(3)	0.04
2004dt	-7.8	10325(318)	35(4)	16082(407)	42(4)	21199(484)	20(2)	0
2004eo	-11.4	12500(537)	21(3)	17500(690)	11(2)	24479(948)	1(1)	0.3
2004ey	-8.2	12114(523)	18(2)	17930(698)	13(1)	23000(856)	2(1)	0.05
2005cf	-12.7	11295(513)	7(1)	17213(679)	8(1)	23592(873)	1(1)	0.12
2005cf	-11.7	11186(331)	12(1)	16824(416)	9(1)	22034(494)	4(1)	0.06
2005cf	-11.3	11281(332)	10(1)	17002(418)	8(1)	21877(492)	4(1)	0.05
2005cf	-10.7	11029(498)	8(1)	17242(681)	5(1)	23016(857)	2(1)	0.08
2005cf	-9.7	10968(329)	8(1)	16782(416)	6(1)	22383(499)	3(1)	0.08
2005cf	-8.7	10774(485)	10(1)	16315(658)	8(1)	22081(831)	5(1)	0.1
2005cf	-7.7	10334(322)	14(2)	16334(410)	8(1)	21827(489)	7(1)	0.12
2005cg	-9	11555(509)	15(2)	18000(704)	5(1)	22210(831)	2(1)	0
2005el	-8.1	11000(460)	31(2)	17078(416)	14(2)	22511(503)	4(1)	0.04
2005el	-7.1	11000(480)	31(3)	17171(672)	12(1)	22067(818)	3(1)	0.03
2005el	-6.9	11000(491)	31(3)	16555(418)	12(1)	21000(488)	4(1)	0.02
2005eu	-9.1	12447(535)	5(1)	18782(728)	2(1)	23200(862)	4(1)	0
2006X	-11.1	15500(660)	5(1)	21000(798)	24(3)	24040(527)	7(1)	0
2006X	-6.8	15579(398)	14(1)	20536(474)	24(2)	24008(856)	1(1)	0
2006ax	-10.8	11500(506)	22(2)	16200(650)	9(2)	21410(812)	2(1)	0.03
2006ax	-10.4	10622(474)	25(3)	17102(674)	11(1)	22864(851)	2(1)	0
2006ax	-8.8	10493(466)	16(2)	16630(650)	12(2)	21959(795)	2(1)	0
2006dd	-12.4	11156(341)	21(2)	17280(427)	12(2)	22309(502)	6(1)	0.22
2006dm	-7.9	10000(460)	55(6)	16351(653)	23(3)	21000(795)	7(1)	0
2006dy	-11.8	10556(491)	38(4)	18317(722)	8(1)	22949(842)	2(1)	0.08
2006gr	-9.2	13100(556)	8(1)	19269(744)	7(1)	23148(860)	3(1)	0
2006kf	-8.3	11991(460)	64(4)	17418(673)	21(3)	22152(830)	6(1)	0.04

Table 2
(Continued)

SN	t^a (day)	V_P^b (km s ⁻¹)	W_P^c (Å)	V_H^d (km s ⁻¹)	W_H^e (Å)	V_S^f (km s ⁻¹)	W_S^g (Å)	R_b^h
2006le	-8.9	12209(524)	9(1)	18176(709)	7(1)	23003(855)	4(1)	0
2007F	-9.7	11868(518)	6(1)	17995(702)	2(1)	22964(843)	2(1)	0
2007af	-11.3	11183(496)	35(3)	17000(674)	19(2)	22091(829)	1(1)	0.11
2007bd	-8.1	11580(508)	39(4)	17500(689)	20(2)	24000(887)	1(1)	0
2007bm	-8.2	11246(507)	36(2)	17170(676)	12(1)	21473(813)	5(1)	0.06
2007ca	-10.4	11000(491)	17(2)	17811(700)	8(1)	23102(859)	1(1)	0
2007ci	-7.1	11614(509)	50(5)	16000(643)	20(2)	22693(845)	6(1)	0
2007le	-10.4	14623(603)	6(1)	20000(766)	2(1)	24000(887)	2(1)	0
2007le	-9.7	14859(616)	9(1)	20142(776)	4(1)	24000(887)	2(1)	0
2007le	-9.5	14618(602)	15(2)	21000(797)	4(1)	24000(887)	5(1)	0
2008ar	-9.2	12414(535)	11(1)	17264(682)	10(1)	21827(820)	3(1)	0
2008ar	-9.1	12000(522)	14(1)	17026(666)	4(1)	21518(818)	3(1)	0
2008bc	-9.7	14337(606)	15(2)	19000(736)	6(1)	23364(865)	5(1)	0.09
2008bf	-9.5	12000(522)	14(2)	18677(723)	5(1)	24010(886)	2(1)	0
2008hv	-11.3	14314(375)	36(3)	18500(721)	9(1)	22505(503)	2(1)	0.2
2009aa	-8.7	10381(481)	28(2)	16824(683)	13(1)	22255(829)	1(1)	0
2009aa	-7.7	9588(450)	29(3)	16000(643)	16(2)	21621(814)	2(1)	0
2009ab	-10.8	11303(335)	30(2)	17730(428)	16(2)	23107(512)	5(1)	0.21
2009dc	-7	9000(430)	47(5)	16984(673)	14(2)	21000(795)	2(1)	0
2009ig	-14.4	15519(630)	3(1)	21500(813)	1(1)	24145(891)	1(1)	0
2009ig	-12.5	15500(630)	2(1)	21000(797)	1(1)	24192(891)	1(1)	0
2009ig	-11.5	15682(635)	2(1)	20728(694)	2(1)	24000(887)	2(1)	0
2009ig	-9.5	15000(614)	8(1)	18284(440)	4(1)	22689(506)	6(1)	0
2009ig	-8.5	14845(387)	8(1)	19000(736)	2(1)	24000(887)	3(1)	0
2011by	-12.4	11418(333)	30(2)	18592(443)	10(1)	23001(511)	1(1)	0.04
2011by	-7.3	11344(331)	18(1)	17637(430)	12(1)	22110(498)	7(1)	0.03
2011df	-9	13711(574)	9(1)	18615(722)	6(1)	21961(825)	3(1)	0
2011fe	-16	14347(603)	40(3)	19310(749)	16(1)	24242(854)	1(1)	0
2011fe	-15	13439(363)	28(4)	18542(448)	10(1)	23389(518)	3(1)	0
2011fe	-14	12367(350)	33(3)	18500(443)	15(1)	23361(514)	2(1)	0
2011fe	-13	12015(351)	34(2)	18086(437)	12(1)	23451(517)	1(1)	0
2011fe	-12	11936(519)	33(2)	18022(706)	10(1)	22445(840)	3(1)	0
2011fe	-11	10849(486)	39(4)	17647(691)	14(2)	22611(844)	3(1)	0
2011fe	-10	10800(485)	35(3)	17522(689)	13(1)	22379(837)	2(1)	0
2011fe	-9	10819(323)	27(2)	17183(421)	14(1)	21868(492)	6(1)	0
2011fe	-8	11163(331)	26(1)	17082(420)	10(1)	21392(487)	3(1)	0
2011fe	-7	10797(476)	26(3)	16748(678)	14(1)	21663(809)	6(1)	0.01
2012cg	-13.3	12719(544)	22(2)	18500(720)	13(1)	23144(860)	1(1)	0
2012cg	-11.6	12737(544)	19(2)	17685(695)	14(1)	22200(832)	3(1)	0
2012cg	-10	11266(338)	16(2)	17726(436)	8(1)	23564(517)	2(1)	0
2012cg	-8.6	11360(513)	13(1)	17739(703)	9(1)	23356(868)	4(1)	0
2012cg	-8.3	11326(332)	12(1)	17667(429)	7(1)	23038(512)	4(1)	0
2012et	-8	13550(525)	27(3)	18500(720)	11(2)	23043(948)	9(1)	0
2012fr	-12.5	14500(599)	1(1)	21000(797)	3(1)	23269(864)	4(1)	0
2012fr	-11.5	14208(645)	1(1)	19312(747)	3(1)	26000(948)	2(1)	0
2012fr	-8.3	13672(572)	2(1)	18971(737)	4(1)	22325(855)	1(1)	0
2012fr	-8	13000(552)	10(1)	17294(425)	5(1)	21000(795)	2(1)	0
2012fr	-7.7	13116(558)	8(1)	18769(729)	3(1)	23500(871)	2(1)	0
2012fr	-7.5	13406(364)	6(1)	19000(736)	5(1)	23500(871)	3(1)	0
2012fr	-6.8	12766(567)	14(1)	18601(730)	7(1)	25802(944)	1(1)	0.03
2012fr	-6.7	12783(563)	13(1)	18740(724)	9(1)	24251(891)	3(1)	0
2013ah	-7	10083(304)	39(4)	19757(462)	18(2)	26000(948)	11(1)	0
2013dy	-15.8	13732(590)	10(1)	18000(705)	7(1)	21752(806)	1(1)	0
2013dy	-12	11147(347)	15(1)	17500(427)	6(1)	23923(526)	2(1)	0.1
2013dy	-10.5	11375(333)	15(2)	17446(427)	8(1)	23378(517)	6(1)	0.06
2013dy	-9.5	10983(328)	17(2)	16873(419)	7(1)	22990(512)	5(1)	0.09
2013dy	-7.5	10781(333)	20(2)	16400(418)	9(1)	21617(495)	5(1)	0.15
2013gs	-9.7	13748(573)	10(1)	19451(741)	5(1)	25227(928)	1(1)	0
2013gs	-8.4	13500(568)	9(1)	18638(439)	8(1)	25356(546)	2(1)	0.19
2013gs	-7.5	13200(559)	21(2)	19742(759)	9(1)	26000(948)	2(1)	0.03
2013gy	-9.1	12106(538)	32(4)	16553(710)	17(2)	21000(911)	3(1)	0.12
2014J	-11	14952(614)	19(2)	21000(797)	7(1)	24000(887)	2(1)	0
2014J	-10	13923(599)	18(2)	18943(752)	7(1)	23000(857)	4(1)	0

Table 2
(Continued)

SN	t^a (day)	V_P^b (km s ⁻¹)	W_P^c (Å)	V_H^d (km s ⁻¹)	W_H^e (Å)	V_S^f (km s ⁻¹)	W_S^g (Å)	R_b^h
2014J	-7.7	13459(379)	23(2)	19514(480)	9(1)	22782(510)	1(1)	0

Notes. Spectral parameters measured for the absorption O I $\lambda 7773$ in the early spectra of SNe Ia. The abbreviations are similar to those used in Table 1, with V, W, P, H, and S representing the velocity, pEW, photospheric component, HVF-I, and HVF-II, respectively. The 1σ uncertainties shown in the bracket are in units of 1 km s⁻¹ and 1 Å for velocity and equivalent width, respectively.

^a Days since the B-band maximum light.

^b Velocity of O I $\lambda 7773$ for the photospheric component.

^c pEW of O I $\lambda 7773$ for the photospheric component.

^d Velocity of O I $\lambda 7773$ for HVF-I component.

^e pEW of O I $\lambda 7773$ for HVF-I component.

^f Velocity of O I $\lambda 7773$ for the HVF-II component.

^g pEW of O I $\lambda 7773$ for the HVF-II component.

^h The blending ratio between the telluric lines and the photospheric component of O I $\lambda 7773$, defined as $\text{pEW}_{\text{blending}}^{\text{telluric}} / \text{pEW}_{\text{PHO}}^{\text{O}}$, where $\text{pEW}_{\text{blending}}^{\text{telluric}}$ is the pEW of the telluric absorptions overlapped by the photospheric component of O I $\lambda 7773$, and $\text{pEW}_{\text{PHO}}^{\text{O}}$ refers to the pEW of the photospheric component of O I $\lambda 7773$.

Table 3
Fit Results of C II $\lambda 6580$

SN	t (day)	V (km s ⁻¹)	W (Å)	SN	t (day)	V (km s ⁻¹)	W (Å)	SN	t (day)	V (km s ⁻¹)	W (Å)
1990N	-13.9	13496(675)	8.2(0.9)	2005cf	-12.5	12048(362)	1.4(1)	2008Z	-9.4	14000(700)	7.1(0.8)
1994D	-9.5	13114(396)	3.9(1)	2005cf	-11.7	11886(362)	1.5(1)	2008bf	-9.5	12917(388)	2.7(1)
1994D	-8.5	13060(382)	4.6(1)	2005el	-8.1	12130(364)	4.2(1)	2009F	-5.8	12145(608)	6.2(0.7)
1998aq	-9.9	12072(604)	3.7(0.4)	2005el	-7.1	11791(352)	4(1)	2009dc	-7	10351(314)	5.7(1)
1998dm	-10.9	12580(629)	1.7(0.2)	2005eu	-9.7	12487(625)	2.6(0.3)	2009ig	-15	9304(466)	0.5(0.1)
1999by	-6.2	10454(523)	1.3(0.2)	2005iq	-6.4	11889(595)	3.2(0.4)	2011by	-10	12821(390)	3.1(1)
1999cp	-12	12688(635)	6.3(0.7)	2006D	-6.3	12010(601)	6.8(0.7)	2011fe	-13	11732(360)	3.2(1)
2002cr	-11.3	11007(330)	2.7(1)	2006ax	-11.1	11326(567)	5.2(0.6)	2011fe	-12	11778(354)	2.1(1)
2002cr	-7.6	10563(316)	2.4(1)	2006dd	-12.4	12436(368)	2.9(1)	2011fe	-11	11402(346)	1.9(1)
2003du	-14.1	12722(382)	2.8(1)	2006dy	-11.8	11914(362)	3.1(1)	2011fe	-10	11285(332)	3.6(1)
2003du	-12.8	12392(372)	3.9(1)	2006gz	-9.6	13622(682)	14.6(1.5)	2011fe	-9	11094(334)	2.1(1)
2003du	-12.1	12311(370)	1.9(1)	2006le	-7.9	12284(615)	3.7(0.4)	2011fe	-7	10792(324)	1.8(1)
2003du	-10.8	12221(366)	2(1)	2007F	-9.7	12640(380)	1.2(1)	2012cg	-10	12668(382)	4.9(1)
2003du	-9.9	12009(360)	2.6(1)	2007af	-11.3	12031(366)	1.2(1)	2012cg	-8.6	12400(595)	3.1(1)
2003du	-8.9	12378(372)	2(1)	2007bm	-9.3	11436(344)	2.3(1)	2012cu	-7	12150(608)	8.1(0.9)
2003kf	-9.4	12878(644)	2.4(0.3)	2007bm	-8.5	11260(342)	1.6(1)	2013dy	-15.8	>13000	>20
2004bw	-10.5	12301(616)	10.5(1.1)	2007le	-10.7	13607(681)	0.6(0.1)
2005cf	-12.7	12048(362)	1.4(1)	2008Q	-7.3	14000(700)	6.5(0.7)

Note. Spectral parameters measured for C II $\lambda 6580$ in early spectra of SNe Ia. Velocity is abbreviated to V and pEW is further abbreviated to W due to limited space. The 1σ uncertainties shown in brackets are in units of 1 km s⁻¹ and 1 Å for velocity and equivalent width, respectively.

somehow tied to SN properties. Note that the O-HVF we discuss here refers to the HVF-I marked in Figure 1, and we did not attempt to quantify the correlations of the O-HVF-II with the HVFs of Si (or Ca) because this feature is usually very weak and there are relatively larger uncertainties in measuring its absorption strength.

3.3. Correlations of O I $\lambda 7773$, Si II $\lambda 6355$, and the Ca II NIR Triplet

In our previous study, the HVFs of both Si II $\lambda 6355$ and the Ca II NIR triplet in SNe Ia were systematically examined using their early-phase spectra. While the photospheric velocities were found to be similar between Si II $\lambda 6355$ and the Ca II NIR triplet, the HVF velocity of the latter is higher than the former by about 4000 km s⁻¹. Similarly, although the Ca II NIR triplet has a photospheric strength that is roughly comparable to that of Si II $\lambda 6355$, its HVF is found to be much stronger (by about

six times). Note that these correlations are all positive, meaning that the velocity and strength of these two lines grow/decline in the same direction. These two spectral lines were also found to show similar behaviors as functions of photometric and host-galaxy properties such as $\Delta m_{15}(B)$, $B_{\text{max}} - V_{\text{max}}$ color, host-galaxy type, etc. (see details in Zhao et al. 2015). These results indicate that the amount of Si and Ca in both the photospheric component and HVF forming regions are strongly connected. However, the ratio of Si to Ca is not sensitive to the different burning processes expected in SNe Ia (which is similar to the unburned solar composition), while the ratio of O to Si (or Ca) is expected to be quite different in different layers.

Figure 7 compares the line strengths of O and Si for our sample of SNe Ia. In the left panel one can see that the photospheric components of O and Si are positively correlated and the Pearson coefficient is 0.69 for the Normal SNe Ia. On average, the pEW of O photospheric absorption is found to be

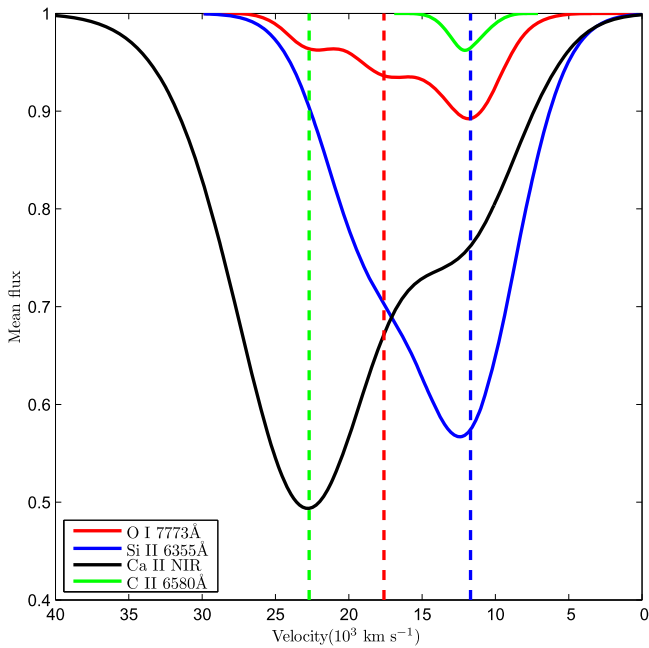


Figure 4. Mean line profiles of the C II $\lambda 6580$ (cyan), Si II $\lambda 6355$ (blue), O I $\lambda 7773$ (red), and Ca II NIR triplet (black) absorption features, obtained with the $t \sim -10$ day spectra of spectroscopically normal SNe Ia, are shown in velocity space. The vertical dashed lines mark the positions of the absorption minima of the HVFs and the photospheric component.

roughly 1/3 times that of Si II. Inspection of the right panel of Figure 7, however, reveals that there is a distinct anti-correlation between the absorption strengths of the HVFs of Normal SNe Ia, with the Pearson coefficient $\rho = -0.71$ for a linear relation. Assuming a reciprocal correlation for the pEW_{HVF}^O-pEW_{HVF}^{Si} relation, the Pearson coefficient becomes 0.90. A similar correlation (for the photospheric components) and anti-correlation (for the HVFs) can also be found between the line strengths of the O I $\lambda 7773$ line and the Ca II NIR triplet lines, as shown in Figure 8, although both these relations are less significant. Compared to Normal SNe Ia, the HV SNe (i.e., $v_0^{\text{Si}} \gtrsim 12,500 \text{ km s}^{-1}$) show large scatter in both Figures 7 and 8, and do not seem to follow well the above relations, in particular the anti-correlation of the HVFs. The spectroscopically peculiar and luminous objects, with weak absorptions of both O and Si, also show obvious deviations in the plots of the HVFs.

The anti pEW_{HVF}^O-pEW_{HVF}^{Si} correlation indicates that, at the outermost layers of the exploding WD, less O will be detected when Si and Ca are more abundant, and this favors the need for oxygen burning to produce the HVFs. Again the HV subgroup of SNe Ia is found to show larger scatter in this correlation, suggesting that the HVFs may have different origins (see discussions in Section 4).

3.4. Correlation of the Absorption with Peak Luminosity

Since the line velocities and strengths of the O I $\lambda 7773$ absorption feature show a wide range for different SNe Ia, it is necessary to explore the reasons for this diversity. Peak luminosity is an important parameter reflecting the properties of SNe Ia. In Figure 9 the observed features of the O photospheric component and O-HVF (including both line velocity and absorption strength) are plotted against the luminosity-indicator parameter $\Delta m_{15}(\text{B})$. As can readily be seen, the velocity of the

O-HVF shows a modest dependence on $\Delta m_{15}(\text{B})$, with slower-declining (or more luminous) SNe Ia having larger ejecta velocities at outer layers. This velocity–luminosity relation can be explained if the characteristic velocity is moved toward higher velocities for explosions with more complete burning. Due to the loss of absorbing oxygen material, the strength of the absorption feature could then be weakened for SNe Ia with higher luminosities. This is supported by the prominent pEW– $\Delta m_{15}(\text{B})$ relation as shown in the right panels of Figure 9, where stronger O I absorptions are found in SNe Ia with lower luminosities. On average, the SNe Ia with $\Delta m_{15}(\text{B}) \gtrsim 1.20$ mag have pEWs that are about 2.0 times larger than those with $\Delta m_{15}(\text{B}) < 1.20$ mag. The above relations become stronger when the HV SNe Ia are discarded in the analysis.

As a comparison, the correlations of Si-HVF and Ca-HVF (line strength and velocity) with $\Delta m_{15}(\text{B})$ are also examined in Figure 10. The velocities of Si- and Ca-HVF are also found to be lower for SNe Ia with larger decline rates, which is similar to the behavior shown by the O-HVF. Although the strength of the Si-HVF does not show a strong anti-correlation with $\Delta m_{15}(\text{B})$, it is clear that stronger Si-HVFs tend to be detected in more luminous SNe Ia (i.e., with $\Delta m_{15}(\text{B}) < 1.3$ mag). This tendency is consistent with the earlier result obtained using the relative line strengths of the Si- and Ca-HVFs (Childress et al. 2014; Silverman et al. 2015; Zhao et al. 2015). The correlation between the Si-HVF and $\Delta m_{15}(\text{B})$ is weaker than that observed between the O-HVF and $\Delta m_{15}(\text{B})$, which may be due to the fact that not all luminous SNe Ia have prominent Si-HVFs, and also that the line blending of the HVF and the photospheric component is more serious than that for the O I $\lambda 7773$ absorption. The fact that the Si-HVF and O-HVF show an opposite correlation with Δm_{15} suggests that the ionization effect should not play a key role in forming the HVFs in the outer layers of the ejecta since Si and O have similar ionization energies (see detailed discussions in Section 4.1).

4. DISCUSSION

4.1. Origin of the HVFs

The origin of the HVFs in SNe Ia still remains unclear. It has been suggested that HVFs could be associated with abundance enhancement (AE), density enhancement (DE), or ionization enhancement (IE) in the outermost layers (Gerardy et al. 2004; Mazzali et al. 2005b, 2005a; Blondin et al. 2012). The material producing the HVFs could either be intrinsic to the SNe or from the CSM. The features we investigate in this work, i.e., O I $\lambda 7773$, Si II $\lambda 6355$, and the Ca II NIR triplet, are suited to probing the density structure (through the pEW), velocity distribution (see Figure 4), and composition (through the pEW) of the ejecta. With this information we may decode the main functions involved in the origin of some HVFs.

Here we briefly summarize the scenarios proposed so far for the formation of HVFs. In the AE scenario, the abundances of Si and Ca are somehow enhanced in the outermost regions of the ejecta. A possible cause is a strong asymmetry in the explosion process (see Maeda et al. 2010 and Seitzzahl et al. 2013 for the single-detonation scenario, or Röpke et al. 2012 for the double-detonation scenario). Alternatively, the abundances could be enhanced by He burning near the WD surface, as suggested by the double-detonation model (e.g., Fink et al. 2007; Woosley & Kasen 2011). In the DE scenario, the HVFs are suggested to originate in a dense shell of

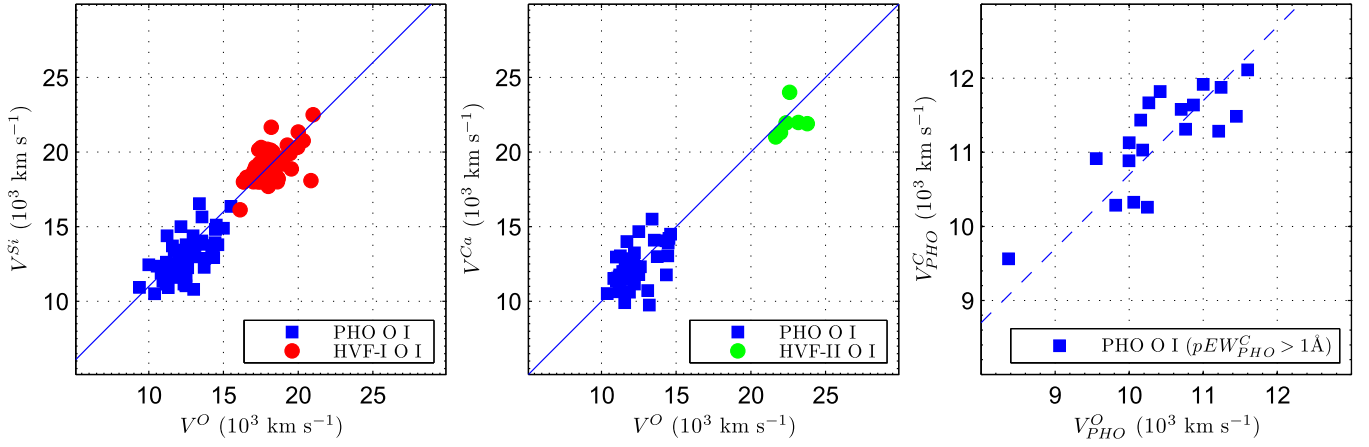


Figure 5. Comparison of velocity inferred from O I line with those from the Si II, Ca II, and C II lines. The blue dots represent the velocities of the photospheric components. The red dots show the Si-HVF and O-HVF-I, while the green dots show the Ca-HVF and the O-HVF-II. Only those spectra with significant detection of the carbon signature are used for comparison with the C II velocity.

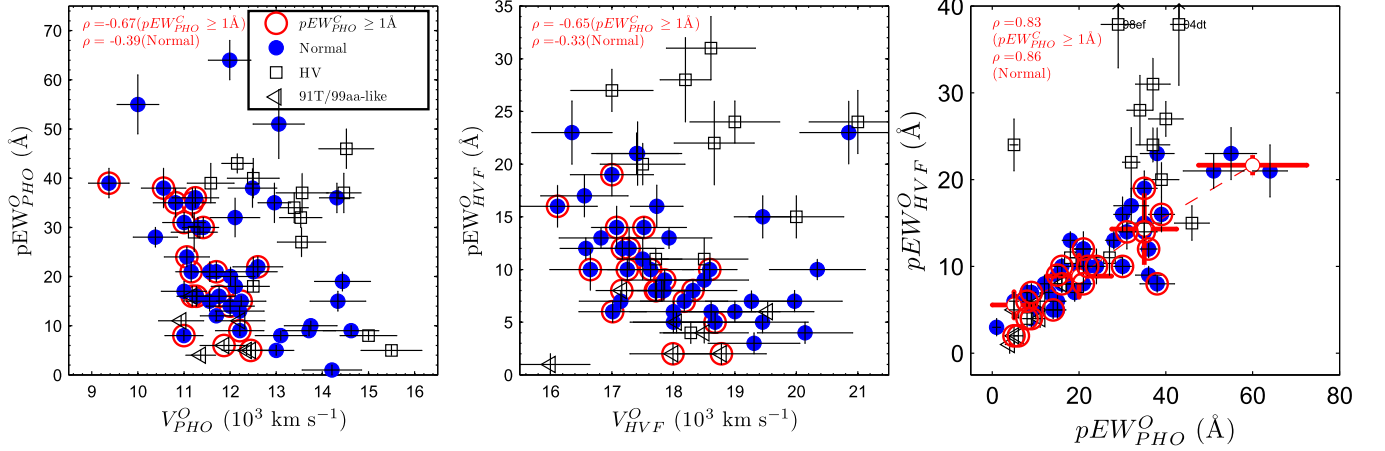


Figure 6. Line strength and velocity of O I $\lambda 7773$. (a) Comparison between the line strength of the photospheric component of O I $\lambda 7773$ absorption and the corresponding line velocity. (b) Similar comparison as (a) but for the line strength and velocity of the O-HVF. (c) Comparison of the line strengths between the HVFs and the photospheric components. Blue dots show Normal SNe Ia with $v_0^{\text{Si}} < 12,500 \text{ km s}^{-1}$ at maximum light. The HV SNe Ia ($v_0^{\text{Si}} \gtrsim 12,500 \text{ km s}^{-1}$ at maximum light) and the 91T/99aa-like SNe Ia are represented by squares and triangles, respectively. The larger red open circles represent the subsample of SNe Ia showing prominent C II $\lambda 6580$ absorption in the early-time spectra, i.e., $pEW > 1.0 \text{ \AA}$ at $t \sim -10$ day.

basically unburned material, formed either at the outermost layer of the ejecta or in the CSM (Gerardy et al. 2004; Mazzali et al. 2005a; Tanaka et al. 2006, 2008; Mulligan & Wheeler 2015). In the IE scenario, a small amount of H in the outermost layer serves as a source of free electrons, which thus suppresses the ionization status of Ca and Si through recombination. This then leads to a larger amount of Ca II and Si II, potentially producing HVFs (Mazzali et al. 2005b; Tanaka et al. 2008). This may happen either as a contamination of H in the WD surface before the explosion or due to an interaction between the ejecta and the H-rich CSM, similarly to the DE scenario.

In our previous study (Zhao et al. 2015), the HVF of Si II $\lambda 6355$ was compared to that of Ca II NIR and was found to be much stronger (the difference in strength could be understood as coming from different ionization potentials and oscillator strengths of the two lines). We also found an anti-correlation with $\Delta m_{15(B)}$, namely slower-declining (or brighter) SNe Ia tend to show more prominent HVFs. In this work, we further examine the behavior and correlations of the fuel-indicative O I $\lambda 7773$ absorption feature. Here we summarize our findings in relation to the expectations from the DE, AE, and IE scenarios.

1. *Mutual correlations of the velocities of HVFs and their time evolutions.* (a) The velocities of the Si-HVFs are about 4000 km s^{-1} lower than the velocities of the Ca-HVFs, i.e., $v_{\text{HVF}}^{\text{Si}} - v_{\text{HVF}}^{\text{Ca}} \approx 4000 \text{ km s}^{-1}$ (see Figure 17 in Zhao et al. 2015). This may not support DE scenario for the origin of HVFs. If the HVFs (of O, Si and Ca) are generated in a dense shell (either the outermost layer of the ejecta or the CSM), their (central) velocities should be roughly the same, regardless of the radiation condition, unless the shell is very thick in radial scale. But such a large-scale DE is not expected in hydrodynamics. Also, the velocities of Si-HVFs are much lower than the expectation from the CSM scenario. As Tanaka et al. (2006) pointed out, dense blobs covering the entire photosphere would result in Si II $\lambda 6355$ absorption velocities in excess of $20,000 \text{ km s}^{-1}$, which is, however, observed in only a few (HV) SNe (see also the discussion in Blondin et al. 2012). (b) Similarly, the time evolution of the line velocities of the O-HVFs as seen in Figure 3 may also not support the DE scenario as the origin of HVFs. If the HVFs originate from a dense shell created

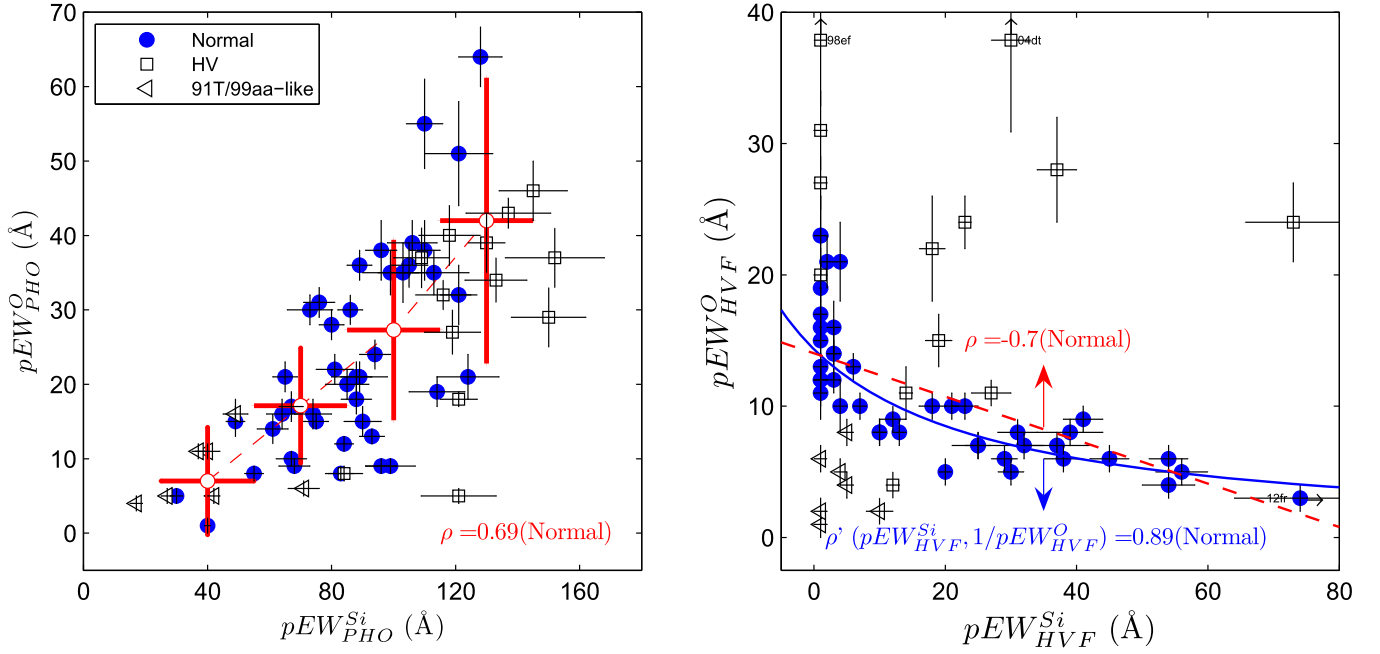


Figure 7. Comparison of the line strength of O I $\lambda 7773$ with that of Si II $\lambda 6355$ for the photospheric components (left) and the HVFs (left). The symbols are the same as in Figure 6. It is clear that the photospheric components of these two features show a positive correlation (with the Pearson coefficient $\rho = 0.69$) and their HVFs have an inverse correlation (with $\rho = -0.70$ for a linear correlation and $\rho = 0.89$ for a reciprocal correlation) for the subgroup of Normal SNe Ia. The open circles in the left panel represent the mean pEWs of O I $\lambda 7773$ in bins of pEWs of Si II $\lambda 6355$, and the error bars are the widths of the bins and 1σ dispersion.

by SN–CSM interaction, one would expect a nearly constant velocity of the HVFs as a function of time, since the hydrodynamical interaction is expected to create a geometrically very thin shell in which the velocity variation is at most a few percent (Chevalier 1982). However, the variation in velocity is much larger, as seen in Figure 3, where the typical velocity variation is close to 20% within one week from the earliest detection.

2. *Additional HVFs of O I $\lambda 7773$.* As one can see from Figures 1, 2, and 4, the HVF of O I $\lambda 7773$ is accompanied by an additional HVF at even higher velocities (i.e., higher by $\approx 4000 \text{ km s}^{-1}$). Possible explanations for this doublet-HVF includes the following. Explanation A—The O-HVF may be a combination of burned and unburned clumps, where the burned clumps also form the Si- and Ca-HVFs. While the detection of Si- and Ca-HVFs suggests that the burnt clumps are distributed in a large velocity space, at higher velocities the fraction of unburned clumps may be large and then the HVF-II of O I may be dominated by such unburned regions. Given the lower ionization energy for Ca II, HVFs can be still formed for the Ca II NIR triplet at higher velocities where a smaller number of burnt clumps exists, but not for Si II. Explanation B—The HVF-II of O I could be produced from carbon burning initiated by outflowing flames at higher velocities (Mazzali et al. 2005b; Maeda et al. 2008) in an asymmetric explosion or from He burning near the WD surface. The burning may also light up the HVFs of Ca II NIR which has a very low excitation energy at early times. However, these processes will not be the dominant factor affecting the correlation with $\Delta m_{15}(B)$ because the amount of helium or carbon near the WD surface is small. Explanation C—The HVF-II of O I could be from a shocked CSM, while the HVF-I is from the outer layers of the ejecta.

3. *Slow time evolution in the line strength of O-HVF.*

For the Normal SNe Ia, the absorption strength of the O-HVF weakens at a much slower rate (see Figure 3) than the Si-HVF in early phases (see Figure 5 in Zhao et al. 2015). This result cannot be explained by the ionization effect because Si II $\lambda 6355$ has an excitation energy even lower than O I $\lambda 7773$ (i.e., 8.12 eV versus 9.15 eV). Nor would this be easy to explain with the DE scenario. If the fast weakening of the Si- and Ca-HVFs is caused by the fast decline of density in the HVF layers, then the O-HVF would also quickly weaken for the same reason. The most plausible explanation could be given by a scenario related to AE. If the abundance of O increases toward lower velocities, then the decreasing density as a function of time could be compensated by the increasing abundance, possibly resulting in a slow evolution. In other words, if the main body of the HVF-I forming region is dominated by the burnt material and these clumps indeed become less significant for the lower velocities toward the photosphere, then the observed behavior is reproduced.

4. *Velocity–pEW correlation of O I absorption.* As can be seen from Figure 6, the line strength of O absorption (both the HVF and photospheric component) is decreasing with increasing velocity. This anti-correlation might be explained by the fact that more complete burning of oxygen could release more energy, driving the remaining oxygen shell to move at a higher velocity. The characteristic velocity is then moved toward higher velocities for explosions with more complete burning. Due to the loss of absorbing oxygen material, the strength of the absorption feature could then be weakened for SNe with higher velocities. This inverse correlation is fully in line with the effect from a burning difference. However, it is not clear why this relation is only strong in the SNe Ia

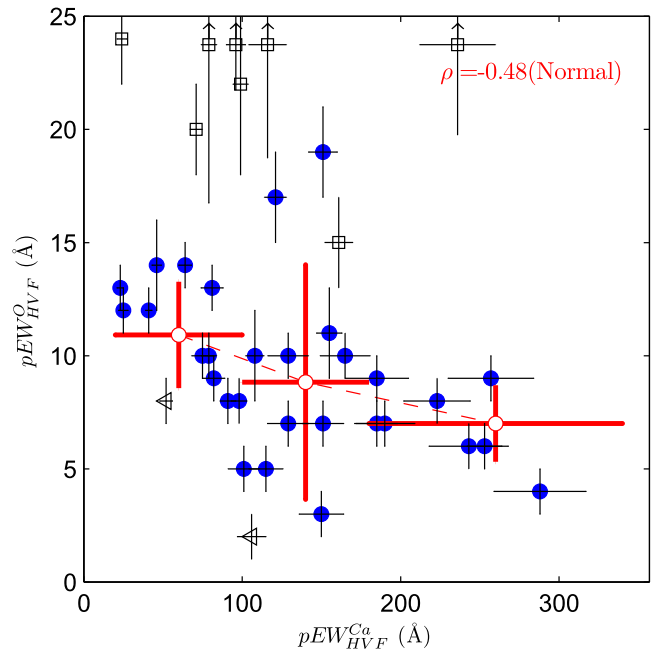
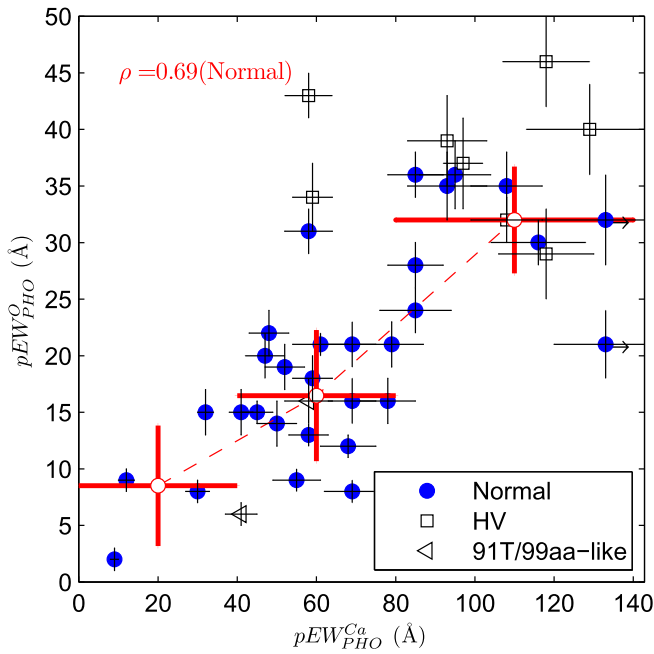


Figure 8. Same as Figure 7 but for a comparison with the Ca II NIR triplet. Similar correlations of the photospheric components and anti-correlations of the HVFs exist between O and Ca, but are less significant compared to those seen between O and Si. The Pearson coefficient is 0.69 for the photospheric component correlation and -0.48 for the HVF anti-correlation. The symbols are the same as indicated in Figure 6.

showing a signature of C II $\lambda 6580$ absorption. Possibly, this indicates that SNe Ia showing strong C II would form a distinct population.

5. *Correlation and anti-correlation between the absorption strengths of O-HVF and Si- or Ca-HVFs.* From Figures 7 and 8, one can see that there are positive correlations between the photospheric components of O and Si (or Ca) and anti-correlations between their HVFs. These results likely provide evidence that the HVF and photospheric component are created at different characteristic burning layers, which is required in the AE scenario. The HVFs of Si and Ca could be produced from He burning or asymmetric burning in the outermost layers. However, this burning process is not expected to have a significant effect on SN Ia luminosity (or $\Delta m_{15}(B)$) due to the small amount of He fuel near the WD surface. Observationally, a SN may show significant deviation from the luminosity- $\Delta m_{15}(B)$ relation established for SNe Ia (Phillips 1993) if the helium burning plays an important role. On the other hand, this relation seems difficult to explain in the DE scenario, as the density of O is also enhanced in the DE process. This finding does not directly support the IE scenario (as such an effect is not required in the IE), but nor does it reject the IE scenario.
6. *Correlation of O-HVF with $\Delta m_{15}(B)$.* From Figure 9, one can see that the strength of the O-HVF tends to become stronger for SNe Ia with larger $\Delta m_{15}(B)$. This tendency is opposite to that seen in the Si-HVF (see Figure 10), where stronger HVFs are only detected in SNe Ia with $\Delta m_{15}(B) < 1.3$ mag. Indeed, the behavior of the O-HVF is understandable through general ionization effects. For the SNe Ia with higher luminosities, the outer materials should be at higher ionization stages. This reduces the number of neutral ions, thus depressing the O I line—as is observed. On the other hand, the behavior seen in Si II is difficult to understand solely from this effect—they

should also be weakened for higher SN luminosity, but the observations indicate the opposite trend. A larger Si/O pEW ratio is observed in our sample for more luminous SNe Ia, a result which solidly rejects the ionization effect as a possible dominant factor.

7. *Abnormal behavior of HV SNe Ia.* Note, however, that the above conclusion may only apply to SNe Ia with relatively lower expansion velocities (i.e., $v_0^{\text{Si}} < 12,500$ km s $^{-1}$) since the HV SNe Ia are found to show significant scatter in the mutual correlations and anti-correlations of line strengths between O and Si (or Ca). Large scatter is also seen in the pEW- $\Delta m_{15}(B)$ correlations (see Figure 9). Thus, an additional mechanism may be needed to explain the formation of the HVFs seen in HV SNe Ia if the measurements of their HVFs are generic. Given that the HVFs of Si in HV SNe have higher velocities than those in Normal SNe, a possible explanation is that the burning effect is weakened as the shells move outward. As an alternative, the HVFs of HV SNe Ia might also arise from the DE of the outer Si shell, perhaps due to CSM interaction. Also, we note that the HV SNe Ia could indeed come from multiple populations, one belonging intrinsically to the same population as Normal SNe (Maeda et al. 2010) and the other exploding in younger environments than Normal SNe (Wang et al. 2013). In this case, it could be natural that the HV SNe show diversity in their HVFs as well. Nevertheless, there remains the caveat that the scatter in the HV SNe Ia could merely arise from the uncertainty in the fitting.

In conclusion, the different behaviors of the HVFs of O and Si (or Ca), in particular the anti-correlations between the HVF strengths, are most naturally explained by a scenario where the HVF regions experience explosive oxygen burning. This result is consistent with, and indeed expected for, the AE scenario.

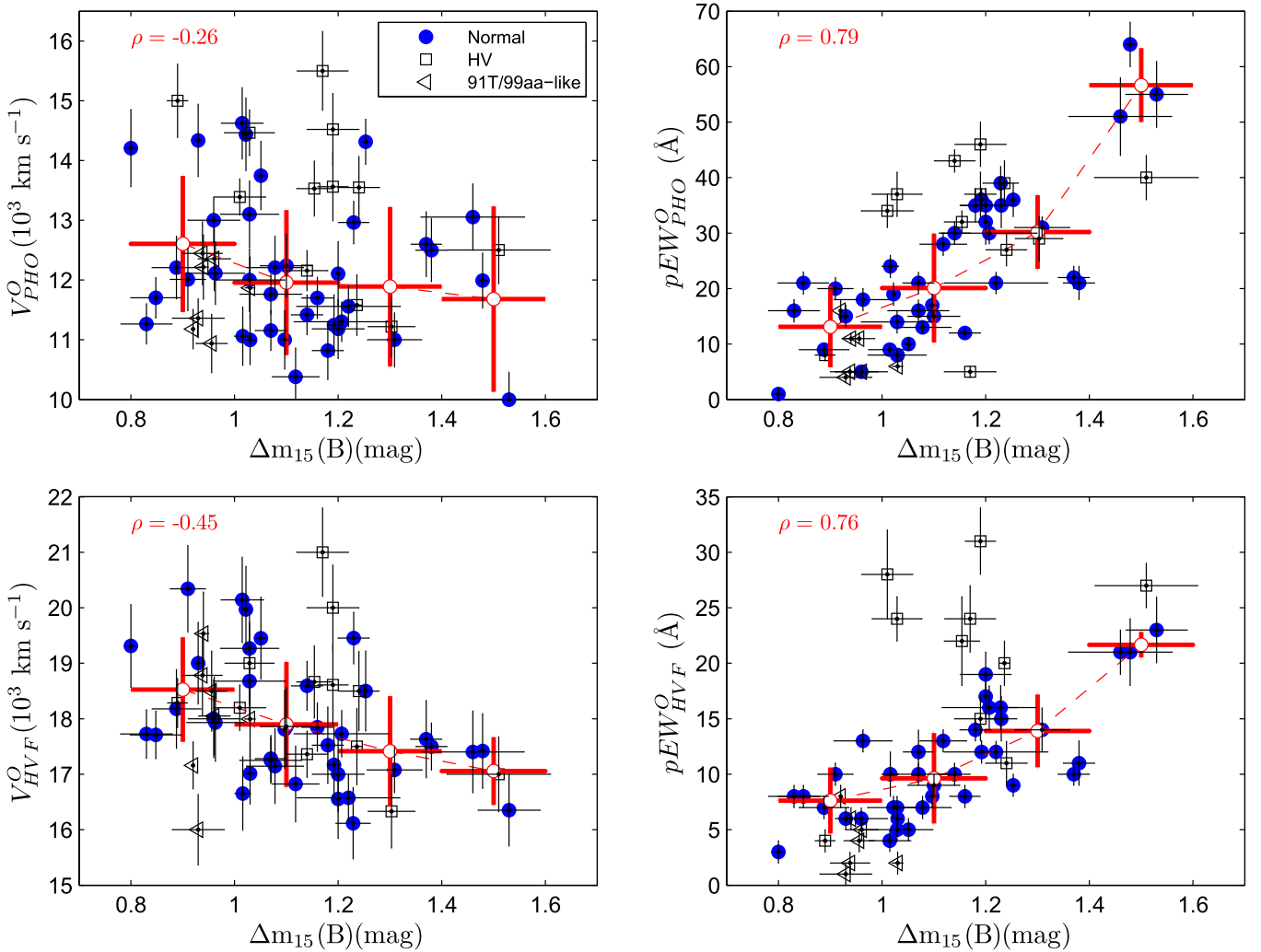


Figure 9. Absorption feature of $O\text{ I } \lambda 7773$ as a function of the luminosity indicator $\Delta m_{15}(B)$ shown for both the photospheric components and the HVFs. SNe Ia with smaller $\Delta m_{15}(B)$ (or higher luminosity) tend to have larger expansion velocities (left panels) but weaker absorptions (right panels). For the photospheric component (upper panels), the Pearson coefficients of these relations derived for Normal SNe Ia are -0.26 for velocity and 0.79 for line strength. For the HVF, the corresponding coefficients are -0.45 and 0.76 for velocity and line strength, respectively. Red circles represent the mean velocity and the pEWs of $O\text{ I}$ absorption in bins of $\Delta m_{15}(B)$, and the error bars represent the width of the bins and 1σ dispersion. The symbols are the same as in Figure 6.

4.2. Constraints on Explosion Models

In addition to clarifying the origin of the HVFs formed at the outermost layers of the exploding WD, our result also places a strong constraint on the still-debated explosion mechanism. The need for the formation of HVFs from nuclear burning leaves us with three possible models: standard delayed detonation (Khokhlov 1991; Gamezo et al. 2005), double detonation through He accretion (Fink et al. 2010; Woosley & Kasen 2011), and the violent merger of two WDs (Pakmor et al. 2011, 2012; Röpke et al. 2012).

It has been suggested that the double-detonation model will mostly produce Fe-peak elements at higher velocities (Woosley & Kasen 2011) rather than intermediate mass elements (IMEs), and C and O will not be present in the He layer. Therefore, this model is not able to explain the HVFs seen at the outermost layers of the ejecta. In the case of violent mergers, the detonation can convert the bulk of the secondary WD to IMEs. The simulation indicates that these IMEs would indeed be left in the low-velocity zone of the ejecta, with typical velocities $< 20,000\text{ km s}^{-1}$ (Röpke et al. 2012), and no mechanism

proposed so far can accelerate the IME-rich region toward higher velocities in this scenario. In addition, for the double-detonation or violent merger models, the “surface” detonation and the resultant HVFs are controlled by the nature of the mass accretion and/or secondary star, while the main features of the SN Ia will be determined by the primary WD. Therefore, it is difficult to understand the luminosity–velocity relation shown in Figures 9 and 10 within the framework of these two models.

On the other hand, the delayed-detonation model has a natural explanation for the observed brighter–faster relation. The diversity of the outer-layer spectral features can be attributed to the difference in the transition density ρ_{tr} from deflagration to detonation in the explosion (Höflich et al. 2002; Woosley et al. 2009). In cases where this transition is delayed, the expansion velocities of the ejecta will decrease and the burned materials like Si (or Ca) will be less abundant at higher velocities because a significant amount of oxygen remains unburned and does not contribute to energy production. This supports the notion that the degree of burning is an important source of spectroscopic diversity among SNe Ia, in addition to progenitor scenarios.

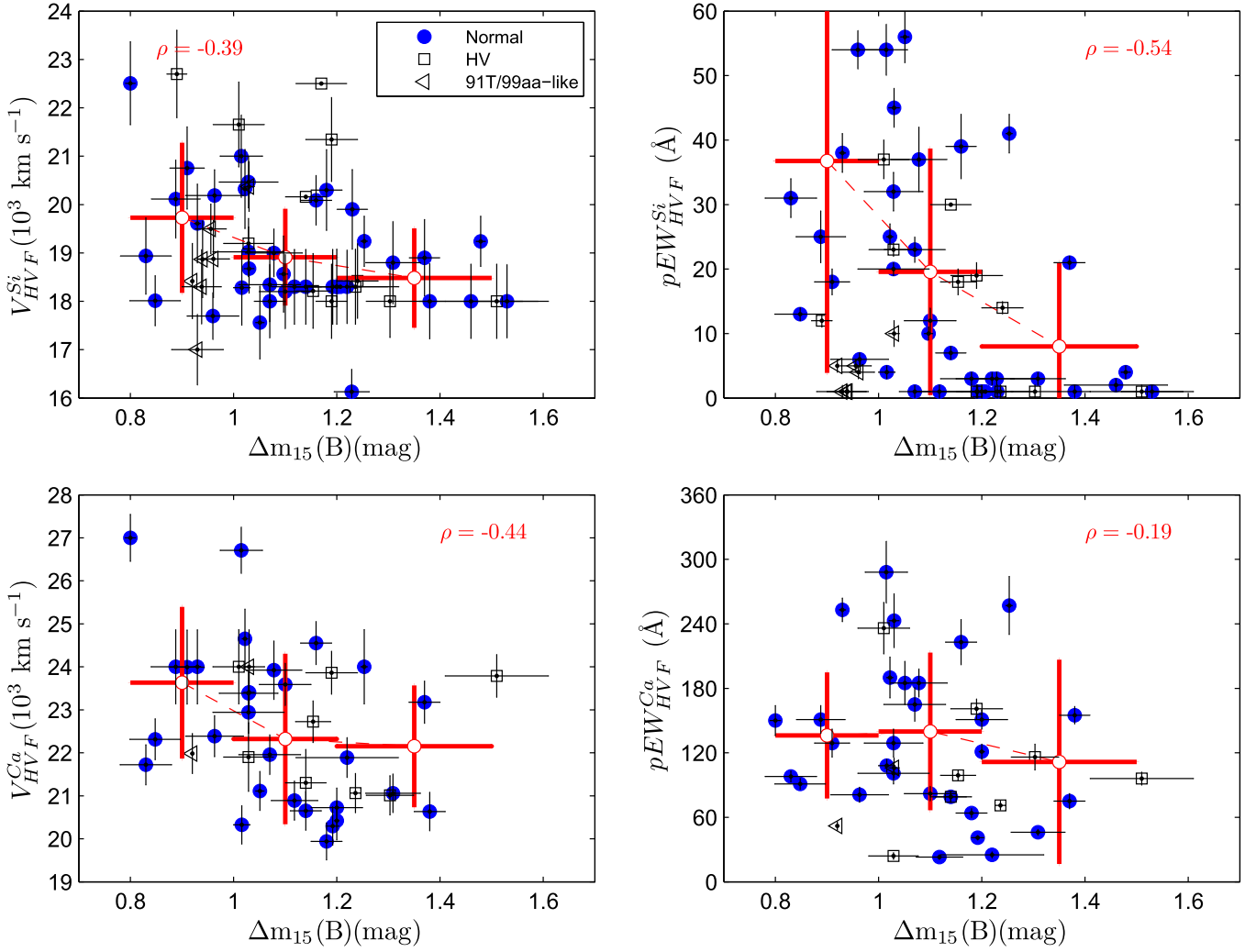


Figure 10. Same as Figure 9 but for correlations of the HVFs of Si II (upper panels) and Ca II (lower panels) with $\Delta m_{15}(B)$.

In the currently available multi-dimensional simulations for delayed-detonation models, the velocity is still limited to $\sim 20,000 \text{ km s}^{-1}$, but this velocity may be further extended once the outermost region is well resolved, and thus higher resolution simulations may show small clumps (currently not resolved) penetrating into the outermost layer. The observed velocity distributions of O and Si, and the Si/O ratio in the outer layers of the ejecta may be used to constrain the density where the transition from deflagration to detonation occurs through comparisons to the predictions from models (Höflich et al. 2002; Seitenzahl et al. 2013). However, high-resolution simulations are further required to provide a guide to connect the detailed hydrodynamic nature of the explosion and the observed properties we have found in this paper.

5. CONCLUSION

With a large sample of early spectra ($t \leq -7$ day), we search for the HVFs in the absorption features of O I $\lambda 7773$, Si II $\lambda 6355$, and the Ca II NIR triplet. Double O-HVFs are detected in the early-time spectra of SNe Ia, with velocities comparable to those of the Si-HVFs and Ca-HVFs, respectively. Their mutual correlations and correlations with $\Delta m_{15}(B)$ are scrutinized.

By comparing the HVFs of O I with those of Si II and Ca II, we attempt to differentiate between various scenarios for the formation of HVFs in the outer layers of the exploding ejecta. From the anti-correlation between the pEWs of the HVF of O I and those of Si II and Ca II, we conclude that oxygen burning is an important contributor to the HVFs of Si and Ca, at least for Normal SNe Ia (see discussion in Section 4.1). This evidence is against the scenario that Si/Ca-HVFs are produced from primordial material (i.e., CSM), while it is in line with the AE scenario. Considering that the HV SNe Ia tend to have distinct explosion environments (Wang et al. 2013; Zhao et al. 2015), and weaker correlations and anti-correlations between O I and Si II (or Ca II), it is possible that the formation of their HVFs is more complicated than that of the Normal counterparts. Indeed the HV subclass may arise from multiple populations, either with a normal-velocity counterpart or without (Maeda et al. 2010; Wang et al. 2013), so this could complicate the analysis of HV SNe Ia. Given that the HVFs of Si in HV SNe Ia have higher velocities than those in Normal SNe Ia, a possible explanation is that the burning effect is weakened as the shells move outward. As an alternative, the HVFs of HV SNe Ia might also arise from the DE of the outer Si shell, perhaps due to CSM interaction.

In addition to distinguishing the origin of the HVFs, the velocities and strengths we have measured for species of C, O, Si, and Ca in this paper could be used to shape a picture of the ejecta, and further constrain the explosion models. The existence of the HVF-I and even the HVF-II of O I $\lambda 7773$ at higher velocities indicates that the photosphere of SNe Ia is covered by oxygen materials (clumps or a separated shell) from the WD and explosive carbon burning. Current observations suggest that the delayed detonation is the favorable explosion model for at least spectroscopically normal SNe Ia with normal photospheric velocities. Numerical explosion simulations with sufficient resolution are encouraged to focus on the outermost layer to further discriminate the explosion models using the new observational indicators we have found in this paper.

We thank the anonymous referee for suggestive comments to help improve the manuscript. The work is supported by the Major State Basic Research Development Program (2013CB834903), the National Natural Science Foundation of China (NSFC grants 11178003 and 11325313), and China Scholarship Council (CSC 201406210312). The work by K.M. is partly supported by JSPS Grant-in-Aid for Scientific Research (No. 26800100) and by World Premier International Research Center Initiative (WPI Initiative), MEXT, Japan. J.Z. is supported by the Key Research Program of the CAS (grant No. KJZD-EW-M06) and the Western Light Youth Project of CAS. This work was partially supported by the Open Project Program of the Key Laboratory of Optical Astronomy, National Astronomical Observatories, Chinese Academy of Sciences. This research has made use of the CfA Supernova Archive, which is funded in part by the US National Science Foundation through grant AST 0907903. This research has also made use of the Lick Supernova Archive, which is funded in part by the US National Science Foundation.

REFERENCES

- Aldering, G., Antilogus, P., Bailey, S., et al. 2006, *ApJ*, 650, 510
 Blondin, S., Matheson, T., Kirshner, R. P., et al. 2012, *AJ*, 143, 126
 Bloom, J. S., Kasen, D., Shen, K. J., et al. 2012, *ApJL*, 744, L17
 Brown, P., Dawson, K. S., Harris, D. W., et al. 2012, *ApJ*, 749, 18
 Chevalier, R. A. 1982, *ApJ*, 258, 790
 Childress, M. J., Filippenko, A. V., Ganeshalingam, M., & Schmidt, B. P. 2014, *MNRAS*, 437, 338
 Cleveland, W. S. 1979, *J. Am. Statist.*, 74, 368
 Contreras, C., Hamuy, M., Phillips, M. M., et al. 2010, *AJ*, 139, 519
 Dilday, B., Howell, D. A., Cenko, S. B., et al. 2012, *Sci*, 337, 942
 Filippenko, A. V., Richmond, M. W., Branch, D., et al. 1992, *ApJL*, 384, L15
 Fink, M., Hillebrandt, W., & Röpke, F. K. 2007, *A&A*, 476, 1133
 Fink, M., Röpke, F. K., Hillebrandt, W., et al. 2010, *A&A*, 514, 53
 Fisher, A., Branch, D., Höflich, P., & Khokhlov, A. 1995, *ApJL*, 447, L73
 Folatelli, G., Morrell, N., Phillips, M. M., et al. 2013, *ApJ*, 773, 53
 Folatelli, G., Phillips, M. M., Morrell, N., et al. 2012, *ApJ*, 745, 74
 Foley, R. J. 2012, *ApJ*, 744, 38
 Gamezo, V. N., Khokhlov, A. M., & Oran, E. S. 2005, *ApJ*, 623, 337
 Ganeshalingam, M., Li, W., Filippenko, A. V., et al. 2010, *ApJS*, 190, 418
 Gerardy, C. L., Höflich, P., Fesen, R. A., et al. 2004, *ApJ*, 607, 391
 Graham, M. L., Foley, R. J., Zheng, W., et al. 2015, *MNRAS*, 446, 2073
 Hachinger, S., Mazzali, P. A., & Benetti, S. 2006, *MNRAS*, 370, 299
 Hamuy, M., Phillips, M. M., Suntzeff, N. B., et al. 2003, *Natur*, 424, 651
 Hatano, K., Branch, D., Fisher, A., Baron, E., & Filippenko, A. V. 1999, *ApJ*, 525, 881
 Hernández, J. I. G., Ruiz-Lapuente, P., Hugo, M. T., et al. 2012, *Natur*, 489, 533
 Hicken, M., Challis, P., Jha, S., et al. 2009, *ApJ*, 700, 331
 Hicken, M., Challis, P., Kirshner, R. P., et al. 2012, *ApJS*, 200, 12
 Hillebrandt, W., & Niemeyer, J. C. 2000, *ARA&A*, 38, 191
 Höflich, P., Gerardy, C., Fesen, R., & Sakai, S. 2002, *ApJ*, 568, 791
 Hsiao, E. Y., Burns, C. R., Contreras, C., et al. 2015, *A&A*, 578, 9
 Iben, I., & Tutukov, A. V. 1984, *ApJS*, 54, 355
 Jha, S., Kirshner, R. P., Challis, P., et al. 2006, *AJ*, 131, 527
 Khokhlov, A. M. 1991, *A&A*, 245, 114
 Krisciunas, K., Suntzeff, N. B., Candia, P., et al. 2003, *AJ*, 125, 166
 Li, W., Bloom, J. S., Podsiadlowski, P., et al. 2011, *Natur*, 480, 348
 Li, W., Filippenko, A. V., Treffers, R. R., et al. 2001, *ApJ*, 546, 734
 Lira, P., Suntzeff, N. B., Phillips, M. M., et al. 1998, *AJ*, 115, 234
 Livne, E., & Glasner, A. S. 1990, *ApJ*, 361, 244
 Maeda, K., Benetti, S., Stritzinger, M., et al. 2010, *Natur*, 466, 82
 Maeda, K., Kawabata, K., Mazzali, P. A., et al. 2008, *Sci*, 319, 1220
 Maguire, K., Sullivan, M., Ellis, R. S., et al. 2012, *MNRAS*, 426, 2359
 Maguire, K., Sullivan, M., Pan, Y.-C., et al. 2014, *MNRAS*, 444, 3258
 Maguire, K., Sullivan, M., Patat, F., et al. 2013, *MNRAS*, 436, 222
 Maoz, D., Mannucci, F., & Nelemans, G. 2014, *ARA&A*, 52, 107
 Marion, G. H., Brown, P. J., Vinkó, J., et al. 2016, *ApJ*, 820, 92
 Marion, G. H., Vinkó, J., Wheeler, J. C., et al. 2013, *ApJ*, 777, 40
 Matheson, T., Kirshner, R. P., Challis, P., et al. 2008, *AJ*, 135, 1598
 Mattila, S., Lundqvist, P., Sollerman, J., et al. 2005, *A&A*, 443, 649
 Maund, J. R., Höflich, P., Patat, F., et al. 2010, *ApJL*, 725, L167
 Mazzali, P. A., Benetti, S., Altavilla, G., et al. 2005a, *ApJL*, 623, L37
 Mazzali, P. A., Benetti, S., Stehle, M., et al. 2005b, *MNRAS*, 357, 200
 Mulligan, B. W., & Wheeler, J. C. 2015, arXiv:1505.05145
 Nomoto, K. 1982, *ApJ*, 253, 798
 Nomoto, K., Iwamoto, K., & Kishimoto, N. 1997, *Sci*, 276, 1378
 Nomoto, K., Thielemann, F. K., & Yokoi, K. 1984, *ApJ*, 286, 644
 Nugent, P., Sullivan, M., Cenko, S. B., et al. 2011, *Natur*, 480, 344
 Pakmor, R., Hachinger, S., Röpke, F. K., & Hillebrandt, W. 2011, *A&A*, 528, A117
 Pakmor, R., Kromer, M., Taubenberger, S., et al. 2012, *ApJ*, 747, 10
 Parrent, J. T., Thomas, R. C., Fesen, R. A., et al. 2011, *ApJ*, 732, 30
 Patat, F., Chandra, P., Chevalier, R., et al. 2007, *Sci*, 317, 924
 Patat, R., Benetti, S., Cappellaro, E., et al. 1996, *MNRAS*, 278, 111
 Perlmutter, S., Aldering, G., Goldhaber, G., et al. 1999, *ApJ*, 517, 565
 Phillips, M. M. 1993, *ApJL*, 413, L105
 Phillips, M. M., Wells, L. A., Suntzeff, et al. 1992, *AJ*, 103, 1632
 Riess, A. G., Filippenko, A. V., Challis, P., et al. 1998, *AJ*, 116, 1009
 Röpke, F. K., Kromer, M., Seitzzahl, I. R., et al. 2012, *ApJL*, 750, L19
 Schaefer, B. E., & Pagnotta, A. 2012, *Natur*, 481, 164
 Seitzzahl, I. R., Ciaraldi-Schoolmann, F., Röpke, F. K., et al. 2013, *MNRAS*, 429, 1156
 Shen, K. J., & Bildsten, L. 2014, *ApJ*, 785, 61
 Silverman, J. M., & Filippenko, A. V. 2012, *MNRAS*, 425, 1917
 Silverman, J. M., Foley, R. J., Filippenko, A. V., et al. 2012a, *MNRAS*, 425, 1789
 Silverman, J. M., Ganeshalingam, M., Cenko, S. B., et al. 2012b, *ApJL*, 756, L7
 Silverman, J. M., Nugent, P. E., Gal-Yam, A., et al. 2013, *ApJS*, 207, 3
 Silverman, J. M., Vinkó, J., Marion, G. H., et al. 2015, *MNRAS*, 451, 1973
 Sim, S., Fink, M., Kromer, M., et al. 2012, *MNRAS*, 420, 3003
 Sternberg, A., Gal-Yam, A., Simon, J. D., et al. 2011, *Sci*, 333, 856
 Stritzinger, M., Hamuy, M., Suntzeff, N. B., et al. 2011, *AJ*, 142, 156
 Stritzinger, M., Hamuy, M., Suntzeff, N. B., et al. 2002, *AJ*, 124, 2100
 Tanaka, M., Mazzali, P. A., Benetti, S., et al. 2008, *ApJ*, 677, 448
 Tanaka, M., Mazzali, P. A., Maeda, K., & Nomoto, K. 2006, *ApJ*, 645, 470
 Thomas, R. C., Aldering, G., Antilogus, P., et al. 2011, *ApJ*, 743, 27
 Wang, X., Filippenko, A. V., Ganeshalingam, M., et al. 2009a, *ApJL*, 699, L139
 Wang, X., Li, W., Filippenko, A. V., et al. 2009b, *ApJ*, 697, 380
 Wang, X., Li, W., Filippenko, A. V., et al. 2008, *ApJ*, 675, 626
 Wang, X., Wang, L., Filippenko, A. V., Zhang, T., & Zhao, X. 2013, *Sci*, 340, 170
 Webbink, R. F. 1984, *ApJ*, 277, 355
 Whelan, J., & Iben, I. 1973, *ApJ*, 186, 1007
 Woosley, S. E., & Kasen, D. 2011, *ApJ*, 734, 38
 Woosley, S. E., Kerstein, A. R., Sankaran, V., Aspden, A. J., & Röpke, F. K. 2009, *ApJ*, 704, 255
 Zhang, J., Wang, X., Bai, J., et al. 2014, *AJ*, 148, 1
 Zhang, K., Wang, X., Zhang, J. J., et al. 2016, *ApJ*, 820, 67
 Zhai, Q., Zhang, J. J., Wang, X., et al. 2016, *AJ*, 151, 125
 Zhao, X., Wang, X., Maeda, K., et al. 2015, *ApJS*, 220, 20
 Zheng, W., Silverman, J. M., Filippenko, A. V., et al. 2013, *ApJ*, 778, L15